Protection against EMF Exposures: Safety or Caution

Consideration from the Viewpoint of System of Protection

Masao Taki[1,2*]
[1]Applied Electromagnetic Research Institute, National Institute of Information and Communications Technology (NICT), 184-8795, Koganei, Japan
[2]Faculty of Systems Design
Tokyo Metropolitan University, 192-0397, Hachioji, Japan
*Corresponding author: m_taki@nict.go.jp

Abstract – Different systems of protection have been applied to different types of effects in terms of dose-effect relationship. Protection system against exposures to electromagnetic fields (EMF) have been recognized to be a health threshold based system. There seems a gap between EMF safety and other product safety. This fact raises a question whether there is some implicit optimization in the system of protection against EMF. The author recommends to identify real threshold of health damage and to clarify the cautionary nature of the current guidelines. Exposure assessment should be done considering this nature.

Keywords – electromagnetic fields; systems of protection; uncertainty

1. Introduction

Exposure assessment is indispensable in any applications of electromagnetic energy. Methods for assessment of electromagnetic fields have been developed with regard to human exposures. PEM technology is expected to make a breakthrough in the measurement instrumentation for this purpose.

The major objective of exposure assessment is to assess the compliance of products or environments with limit values given by exposure guidelines. Difficulties are in the large uncertainty in the compliance assessment. The uncertainty in the compliance assessment comprises of measurement instrumentation uncertainty (MIU) and intrinsic uncertainty of measurand (IUM) [1]. The latter is significantly large in exposure compliance assessment as well as the EMC emission compliance assessment. It is difficult to decide to what extent the measurand uncertainty should be taken into account.

It is warranted to go back to the philosophy of protection behind the exposure guidelines when we discuss this problem. I would like to present my personal view on the required strictness of exposure assessment in consideration of the philosophy of protection against exposure to electromagnetic fields.

2. EMF and Safety

Safety is a mandatory requirement for any product or environment. Safety is defined as “freedom from risk which is not tolerable” according to the definition in ISO/IEC Guide 51 [2], which provides guidance on the inclusion of safety aspects in standards developed by ISO/IEC. Here risk is defined as the combination of occurrence of harm and the severity of that harm, where harm is defined as injury or damage of people, or damage to property or the environment.

Those definitions are of importance when we discuss safety of electromagnetic field (EMF) exposures. We need to identify what is the intolerable risk and the harm which may be caused by EMF exposures.

Current guidelines to limit exposures to EMF are based on the short-term exposure effects. Those are stimulation effect for low frequency region and thermal effect for high frequency region.

Advisory Committee on Safety (ACOS) of IEC published IEC Guide 104 “The preparation of safety publications and the use of basic safety publications and group safety publications (Ed..4.0)” in 2010 [3]. This document provides explanations of safety aspects of electrical equipment as a normative annex. Electrical hazards and temperature hazards are included in the list of hazards that shall be protected. Those are common safety aspects among most of electrical equipment. Their harms are reasonably judged whether tolerable or not.

Non-ionizing radiation, including EMFs, is also listed as one of safety aspects. It is interesting to note that the annex reads “non-ionising radiations generated by the equipment are *limited to the extent necessary for its operation*, and operate at a safe level”.

It should be noted that the treatment of EMF safety is different from those of electrical safety and temperature safety though the established EMF effects are stimulation and heating. Requirement to limit the level to the extent necessary for its operation sounds quite different from requirement for safety or freedom from risk which is not tolerable. It is more like a cautionary approach described in the following.

The Guide 104:2010 has recently been revised [4] and the Annex A (Normative) described above has disappeared.

3. System of Protection

Protection against radiation should be managed based on the characteristic of the dose versus effect relationship. Three types of protection systems exist [4].

First is the health threshold based system. This system is applied to deterministic effect with threshold below which the effect is negligible. Exposure limit is determined based on the threshold with a relevant safety factor. This system of protection should be organized based strictly on scientific considerations without any social and economic factors.

Second is optimization of a known and accepted hazard. This system of protection is applied typically to a stochastic effect with substantial plausibility of the absence of threshold. Delayed effect of low level ionizing radiation is a typical example. Optimization is an approach to manage this type of exposure. Exposure should be kept as low as reasonably achievable (ALARA) as there is no threshold of the effect. In other words, exposure is managed with limits determined by optimization of the trade-off between benefit and cost of reducing the risk. It should be noted that social and economic factors are taken into account to determine optimized exposure limits as cost and benefit are determined in consideration of social and economic factors.

Third is the protection against hazards or risks that are uncertain. ALARA or optimization principle is often considered applicable to this type of possible hazard but it is not correct because there are no criteria available to optimize the cost and benefit because of the absence of knowledge about reduction of risk expected by the reduction of exposure. It should be noted that uncertain effects are substantially different from stochastic effects. Stochastic behavior and uncertainty of risk should not be confused.

4. Protection against EMF Exposures

Health effects of EMF exposures are divided into two categories; short-term effects and long-term effects. The former is deterministic effects and the threshold system of protection is applied. ICNIRP [5] and IEEE/ICES [6] derives their exposure limits based on the threshold of effects.

The latter, long-term effects, includes possible carcinogenicity of ELF and RF EMFs suggested mainly from epidemiological studies. The evidence of causality between exposure and disease is weak and the effect is uncertain. Exposure limits given by ICNIRP and IEEE/ICES do not use those uncertain effects in the derivation of exposure limits.

Here I would like to raise two questions. First is whether the threshold for EMF protection is consistent with other safety aspects such as electrical safety and temperature safety. ICNIRP’s draft RF guideline proposed a concept of “operational adverse health effect threshold”, which appeared to be far from the threshold of intolerable risk, such as that of stimulation or temperature elevation.

Second question is whether current EMF limits really exclude optimization of uncertain effects of long-term exposures. It is true that the exposure limits are explained as threshold based and uncertain effects are not taken into account by ICNIRP as well as IEEE/ICES. In my personal view, however, some optimization should implicitly be applied in the threshold identification and the safety factor to derive the EMF exposure limits.

5. Discussion

Current EMF exposure guidelines have evolved in the history since 1950’s and now play stable roles in sound use of EM energy applications. The framework should be maintained. Nevertheless, I would like to propose some new approaches to clarify sound ways of using current EMF guidelines.

First we need to identify the real thresholds of intolerable health risks, not just “operational thresholds”. This safety threshold should include temporal factors. The ICNIRP ELF guidelines request to limit exposure with instantaneous (<100 μs) levels considering the instantaneous nature of stimulation effect. More duration of exposure, however, should be acceptable at the level of “operational threshold” in the ICNIRP guidelines. We experience transient shock of electrostatic discharge in daily lives. Repeated or continual exposures above the operational threshold should be intolerable but transient and occasional experience of such exposure should be less than intolerable or health threatening experience.

I will be useful to identify the real hazard threshold to manage safety of occupational exposure.

The real threshold is crucially important when we introduce functional safety means in the ELF/IF applications by shutting down the field when a human body approaches unexpectedly close to the source. Real threshold must be identified in consideration of duration of exposure. The data will be useful to determine how fast the functional safety measure is activated.

Second, we need to visualize the implicit optimization included in the current exposure limits. The real safety threshold will be sure to provide exposure limits higher than current limits, which were the result of optimization considering uncertain effect implicitly.

It is reasonable to keep current guidelines levels as the use of current guidelines are well established. But I propose to clarify the current guideline is rather cautionary and safety limit based of real threshold should be given separately. Two different natures should be operated separately between safety limits and cautionary limits.

Regarding the aspect of measurement and assessment, separation of the concept between safety and caution will clarify the relevant approaches to deal with uncertainty.

Compliance of products with standards should be judged in consideration of standards compliance uncertainty (SCU), which is composed of measurement instrumentation uncertainty (MIU) and intrinsic uncertainty of the measurand (IUM).

Compliance with safety standards must take the SCU into account and conservative assessment is required. In contrast the assessment of conformity with cautionary limits may be more flexible. Consideration of MIU is of more priority than UIM for cost effectiveness. This concept of MIU based assessment has been proposed in CISPR 16-4-2 by CISPR SC/A [1] for compliance assessment of electromagnetic compatibility (EMC). Cautionary limits do not directly mean the limit of threat health damage but it is a consensus level considering uncertain effects.

The PEM technical group is expected to improve MIU of EMF exposure assessment drastically. The EMF exposure assessment suffers from difficulty of explosive UIM issues. However, reduction of MIU should be of priority in consideration of the cautionary nature of current exposure limits.

6. Conclusion

In conclusion I would like to recommend the followings.

Identify real threshold of health damage. The threshold should be dependent on exposure duration. This is especially important for low frequency EMF exposures.

Clarify the cautionary nature of the current guidelines. Current exposure limits (or even lower limits) may be justified considering the cautionary nature. However, recognition of real hazard threshold is important.

Simplify the exposure assessment. The limits values are rather cautionary. Too much effort to reduce UIM does not make benefit of health protection but just increases the cost. Efforts should be made on reduction of MIU.

References

[1] CISPR 16-4-2:2011, Specification for radio disturbance and immunity measuring apparatus and methods - Part 4-2: Uncertainties, statistics and limit modelling - Measurement instrumentation uncertainty

[2] ISO/IEC Guide 51:2014, Safety aspects Guidelines for their inclusion in standards

[3] IEC GUIDE 104:2010, The preparation of safety publications and the use of basic safety publications and group safety publications.

[4] IEC GUIDE 104:2019, The preparation of safety publications and the use of basic safety publications and group safety publications

[5] Bergquist U. Development of Guidelines and Standards and thr Principle of ALARA and Prudent Avoidance. R. Matthes (Ed.) Non-Ionizing Radiation, Proc. 3rd International Non-Ionizing Radiation Workshop, ICNIRP 1996, pp.359-372.

[6] ICNIRP Guidelines for Limitting Exposure to Time Varying Electric and Magnetic Fields (1 Hz – 100 kHz),
HEALTH PHYSICS 99(6):818 ‐ 836; 2010

[7] IEEE Standards Coordinating Committee 39 , IEEE Standard for Safety Levels with Respect to Human Exposure to Electric, Magnetic, and Electromagnetic Fields, 0 Hz to 300 GHz, IEEE Std C95.1™-2019

Optical Head for EMC - A Miniature Optical DC to 1 GHz Differential Voltage Probe System

Sven Kuehn[1,2*], Oliver Munz[1], Beyhan Kochali[2] , and Niels Kuster[2]
[1]Schmid&Partner Engineering AG, 8004 Zurich, Switzerland
[2]IT'IS Foundation, ETH Zurich, 8004 Zurich, Switzerland
[*]Corresponding author: kuehn@itis.swiss

Abstract – This paper presents a novel micro-photonic radio-frequency differential voltage probe able to acquire the full complex-valued voltage signal under electromagnetically hostile exposure conditions. The probe system design supports a frequency range from a few Hertz up to 1 GHz, with a sensitivity of $100\,\mu\mathrm{V}/\sqrt{Hz}$ 110 dB dynamic range and a frequency response of $< \pm 2$ dB.

Keywords – EMC, differential voltage probe; radio-frequency

1. Introduction

Conducted EMC tests in electromagnetically hostile environments such as electric vehicle drive trains, ignition systems or power transformers can become a challenging if not impossible task for test engineers. In such environments, cable pickup or pickup by the test equipment itself can be significant compared to the measured voltages inside the equipment under test. Further the electrical size of traditional probes makes it more and more challenging to provide a high input impedance up to frequencies as high as 1 GHz. With the RFoF1P4med probe [1] we have developed a differential voltage probe system functional from 10 MHz to 1 GHz with a specific application focus on radio-frequency immunity testing when active medical implants are exposed to the strong radio-frequency magnetic fields inside magnetic resonance imaging system. However, this system design was not able to cover requests from the automotive, power electronics and medical industries to measure voltages with frequencies as low as a few Hertz. With the optical head for EMC (OH4EMC) – Figure 1 – we have addressed these needs by a re-design of our time-domain sensor optical platform to support DC-coupled measurements.

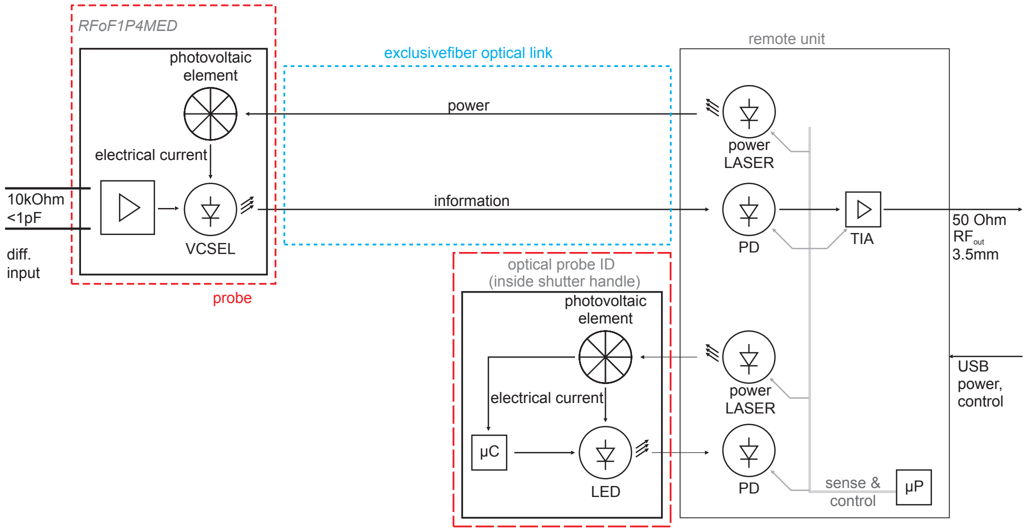

Figure 1. Schematic diagram of the OH4EMC fiber optical differential voltage probe system.

2. System Design

The system (Figure 1) uses direct laser modulation for the transmission of the signals fed to the 300 kΩ, <1 pF differential input of the OH4EMC probe. The OH4EMC probe and the remote unit are exclusively optically linked by fiber-optics. A power laser is used to illuminate a photovoltaic converter inside the probe head via the fiber optics. The electrical energy from the photovoltaic cell drives a small current stabilized laser and a differential amplifier inside the sensor head. The input signal, amplified by the differential amplifier modulates the optical output power of the vertical cavity surface emitting LASER (VCSEL). This signal is then transmitted to the remote unit over an optical fiber. At the remote unit, the optical signal is demodulated again by means of a fast photodiode, and the received signal is amplified by a novel DC-coupled wideband transimpedance amplifier and made available via a standard 50 Ω output to connect to standard test and measurement equipment.

2.1 Transducer Design

The voltage probe electro-optical transducer is designed in a highly symmetric manner as shown in Figure 2. The probe circuitry has a total electrical size of $4\times2\times1\,\mathrm{mm}^3$ including the preci-dip differential connector. In order to reduce parasitic pickup, the connector and electronics are inserted into a brass shield.

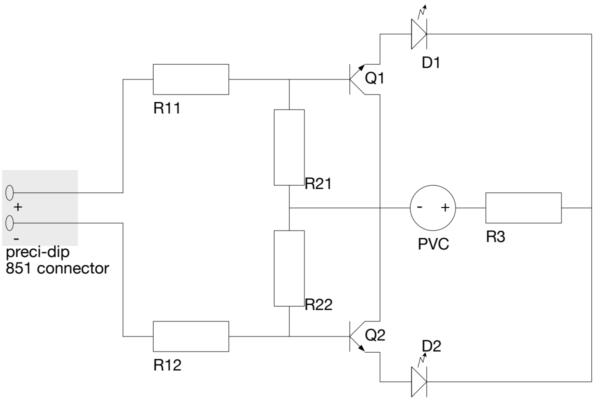

Figure 2. Schematic diagram of the OH4EMC differential active electro-optic voltage probe .

2.2 Receiver Design

The opto-electrical receiver to the probe had to be re-design in order to provide DC coupling. In the presented design (Figure 3) this is achieved by a zeroing switch to determine input bias drifts, a DC setpoint circuitry and a 2 dB attenuator pad in order to protect external equipment.

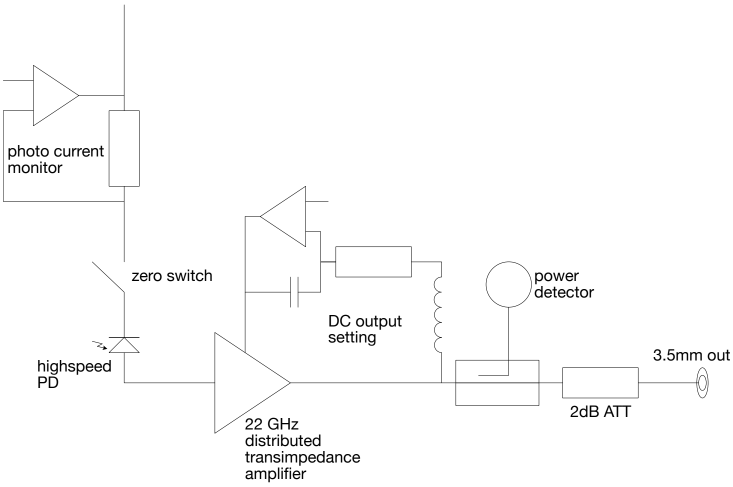

Figure 3. Schematic diagram of the OH4EMC DC-coupled opto-electrical converter.

2.3 Calibration Unit

A battery-powered single-ended to differential calibration unit (Figure 4) has been designed in order to determine the transmission coefficient of the OH4EMC system. Using the calibration unit on-site allows reducing transmission coefficient uncertainties, e.g., due to change of thermal environmental conditions or due to optical connector mating uncertainties. The frequency-dependent transmission coefficient of the calibration unit has to be calibrated (denoted here as T_{CU} in dB). Then the user can determine the transmission of the entire OH4EMC system (T_{OH4EMC} in dB) on-site by measuring the transmission ($T_{calibration}$ in dB) from the single-ended input of the calibration unit to the single-ended output of the remote unit using the following calculation:

$$T_{OH4EMC} = T_{calibration} - T_{CU}\,. \qquad (1)$$

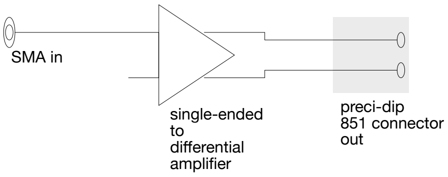

Figure 4. Schematic diagram of the OH4EMC calibration unit for on-site transmission coefficient calibration.

3. Results

We have implemented the novel optical differential voltage probe system in a miniaturized design. Figure 5 shows the prototypes of the developed OH4EMC electro-optical transducer, optoelectric receiver, and calibration unit. The calibration unit is inserted in a shielded housing in order to improve the isolation and phase stability of the calibration unit. The electro-optical transducer and the calibration unit have been equipped with guiding notches in order to protect the sensitive preci-dip 851 connectors. For the system evaluation, the opto-electrical receiver was integrated into a remote unit that also provides the forward photonic power to the OH4EMC opto-electrical transducer.

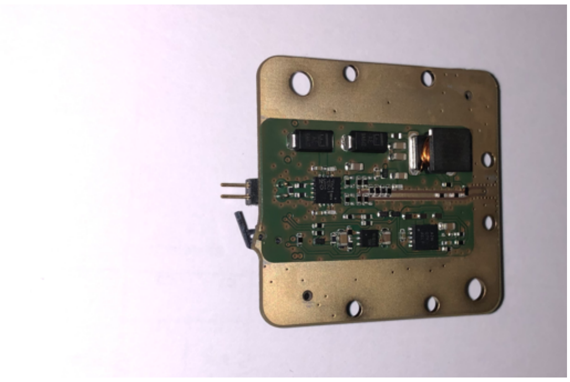

(a) OH4EMC calibration unit electronics.

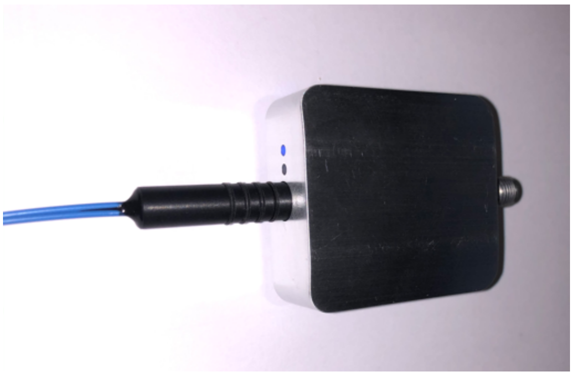

(b) OH4EMC calibration unit final assembly.

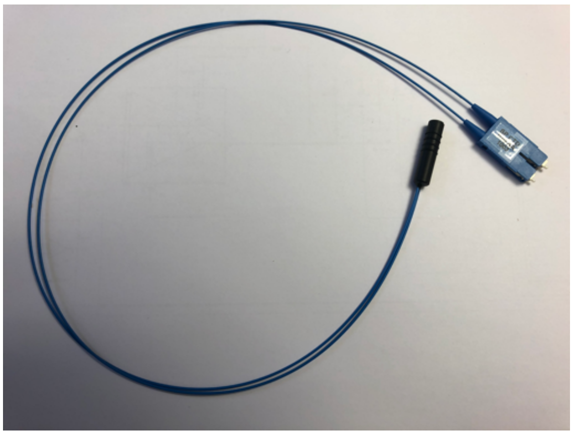

(c) OH4EMC transducer.

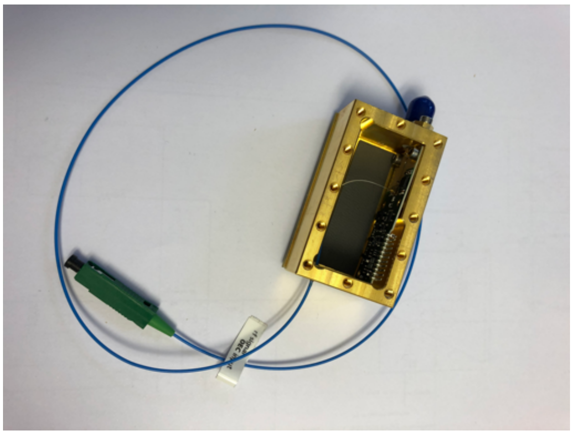

(d) OH4EMC electro-optical receiver.

Figure 5. OH4EMC prototype system.

Figure 6 shows the measurement results for the transmission from 5 Hz to 1000 MHz as well as the noise floor from 10 Hz to 500 MHz. Based on these measurements as well as a dynamic range test and a repeatability evaluation we have determined preliminary specifications as well as a preliminary measurement uncertainty budget. The measurement uncertainty of the differential voltage probe system was found to be as low as 1.14 dB (k=1). The preliminary specifications of the probe system are summarized in Table 1.

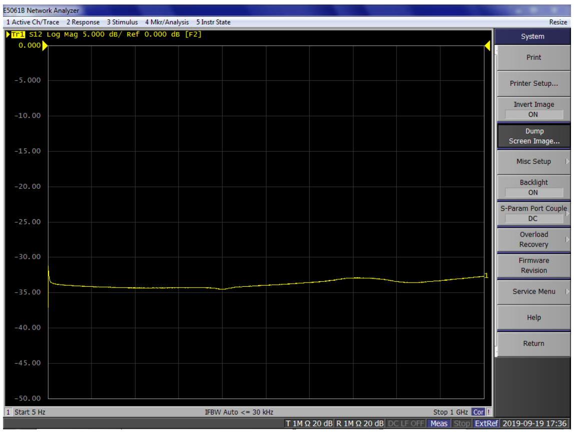

(a) Transmission characteristics of OH4EMC system (calibration unit, electro-optical transducer, opto-electric receiver) measured with a vector network analyser from 5 Hz to 1000 MHz.

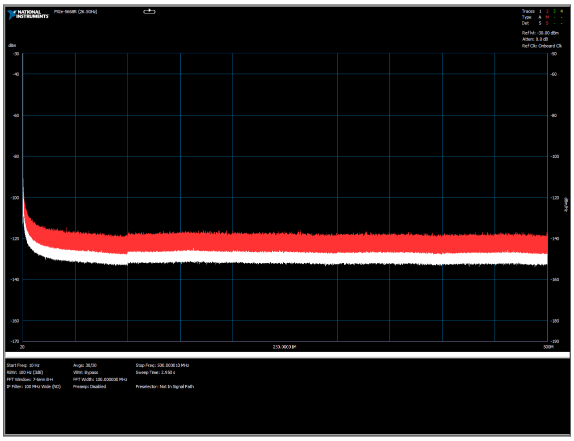

(b) Red curve: Displayed average noise floor (30 averages, 100 Hz resolution bandwidth) from 10 Hz to 500 MHz. White curve: spectrum analyzer displayed average noise floor.

Figure 6. Measurement results for transmission and sensitivity of the OH4EMC prototype.

Table 1. Specification of the developed RFoF1P4MED optical voltage probe system.

Bandwidth(3 dB)		5 Hz – 1 GHz
Signal input		
	Connector	preci-dip 851
	Input impedance	>300 kOhm
	Diff. range	±12 V
	Noise floor	$<100\ \mu V/\sqrt{Hz}$
Signal output		
	probe	MU-duplex
	remote unit	50 Ohm (SMA)

4. Conclusions

This paper presents a novel micro-photonic radio-frequency voltage probe able to acquire the full complex-valued voltage signal under electromagnetically hostile exposure conditions. The novel design allows for DC-coupled measurements from a few Hertz up to 1 GHz with a single probe system. The OH4EMC system is specifically designed for measuring small conducted voltage levels in electromagnetic hostile environments such as electric vehicle drive trains, power converts, ignition systems or magnetic resonance systems. The overall measurement uncertainty was found to be better than 1.14 dB (k=1).

References

[1] Sven Kuehn et al. “In-vitro measurement system for induced voltages in medical implants in magnetic resonance imaging”. In: *2018 IEEE International Symposium on Electromagnetic Compatibility and 2018 IEEE Asia-Pacific Symposium on Electromagnetic Compatibility (EMC/APEMC)*. IEEE. 2018, pp. 80–81.

90GHz-band Foreign Object Debris Detection System and Radar Cross Section Simulation for Runway Surveillance

Nobuhiko Shibagaki

Enterprise System Division,
Hitachi Kokusai Electric Inc.
Kodaira-shi, Tokyo, Japan
shibagaki.nobuhiko@h-kokusai.com

Abstract – Demand for transportation systems using airplanes is rapidly growing in all over the world. Quick and precise detection of foreign object debris (FOD) on the runway is vitally significant to maintain the safe operation of the airdrome. We are trying to establish the new RADAR system which is employing both Radio-over- Fiber technologies and millimeter-wave radar technologies for high-performance and cost-effective foreign object debris detection systems (FODDS). In the radar system under consideration, it is possible to supply, transmission signals from a single signal source to multiple Radar Antenna Units (RAU) using Radio-over-Fiber technology. For this reason, not only the Monostatic radar systems but also Bistatic radar systems can be realized. To evaluate the system performance of the radar system, the radar cross section (RCS) of the foreign object debris on the runway is key parameters. On-site measurement of RCS is difficult in the millimeter-wave band. For this understanding, simulation by electromagnetic field analysis using the Finite Element Method and Integral Equation Method is performed. MonostaticRCS simulation results have employed for the performance evaluation of the practical system. The fundamental research of the Bistatic radar system was carried out using the calculation result of BistaticRCS. As a result, the Bistatic radar system showed superior detection performance than the Monostatic radar system. We introduce the essential performance of the demonstration system installed at Narita and/or Kuala Lumpur international airport along with RCS simulation.

Keywords – radar; millimeter-wave; FOD; RCS

1. Introduction

The demand for transportation systems using airplanes is rapidly growing all over the world. Quick and accurate detection of foreign object debris (FOD) on the runway is vitally important to maintain the safe operation of the airport. We are studying the new RADAR system which is employing both Radio-over-Fiber technologies and millimeter-wave radar technologies for high-performance and cost-effective foreign object debris detection systems (FODDS). In the radar system under consideration, it is possible to supply, transmission signals from a single signal source to multiple Radar Antenna Units (RAU) using Radio-over-Fiber technology. For this reason, not only the Monostatic radar systems but also Bistatic radar systems can be realized. To evaluate the system performance of the radar system, the radar cross section (RCS) of the foreign object debris on the runway is key parameters. On-site measurement of RCS is difficult for the millimeter-wave band. For this reason, simulation by electromagnetic field analysis using the Finite Element Method and Integral Equation Method is performed. MonostaticRCS simulation results have employed for the performance evaluation of the demonstration system installed at Narita International Airport. This study showed that RCS simulation by electromagnetic simulation is useful. Also, the fundamental research of the Bistatic radar system was carried out using the calculation result of BistaticRCS. As a consequence, the Bistatic radar system showed superior detection performance than Monostatic radar system. We present the essential operation of the demonstration system installed at Narita airport along with RCS simulation.

2. System Configuration and RCS

Fig. 1 shows the system configuration of the runway surveillance radar system for FOD detection. The radar performance is essentially defined by the radar equation shown in Fig. 2 and the reception sensitivity of the radar system. Therefore, it is possible to evaluate the detection performance, according to the radar equation of FIG. 2. In order to quantitatively evaluate what can be detected by radar, the radar cross section (RCS) can be the most important parameter if the transmission power, antenna gain, and frequency of utilization are given. Regarding objects with basic shapes such as cylinders or spheres, the RCS can be obtained analytically, but it is necessary to determine the general shape by actual measurement or electromagnetic field analysis. However, it is not easy to measure the RCS of an object in the millimeter-wave band, and the simulation by the electromagnetic field analysis becomes important.

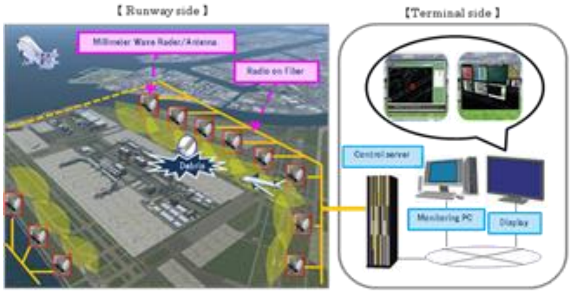

Figure 1. System Configuration.

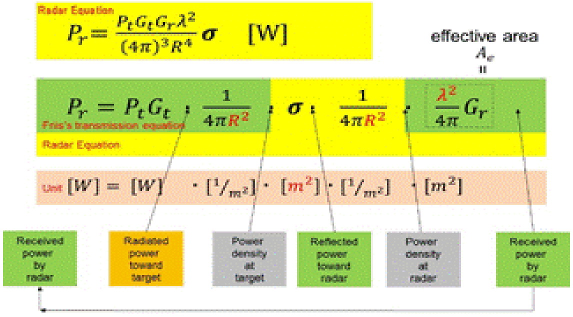

Figure 2. Basic Radar Equation

3. Bistatic Radar System

FIG. 3 is a schematic view of a Bistatic radar system in which the antenna stations A and B share the signal sources via RoF technology.

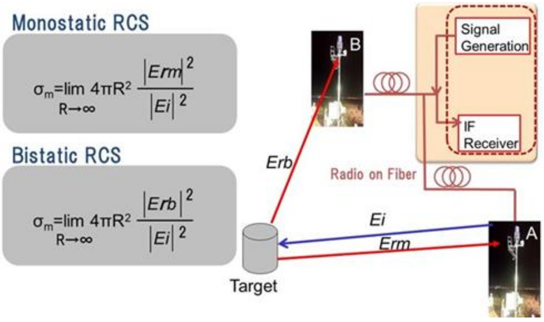

Figure 3. Definition diagram for RCS

As can be seen from the definition of the radar cross section σ in the figure, the RCS is a reflection coefficient unique to the object, the shape, and the material. The Monostatic RCS is a factor indicating how much reflections of a signal incident on an object returns to the incident direction. On the other hand, the Bistatic RCS is an amount in which the incident signal hits the object and reflects in all directions. Therefore the Monostatic RCS is a single value for a single incident direction, and the Bistatic RCS has the 3D direction for a single incidence direction.

4. RCS simulation results

The RCS of the M10 bolt was calculated at 100 GHz by using the finite element method as an example of an object with anisotropic shape. Fig. 4 shows the model used for the simulation and Fig. 5 shows the calculation results of the Monostatic RCS.

As shown in FIG. 6, the BistaticRCS has a different 3D characteristic depending on the incident direction. Thus, yet when the MonostaticRCS is small, a large reflected power may reflect in a direction not in the incident direction. If Bistatic radar is available, it may be possible to observe targets that are not sensitive to reception sensitivity in Monostatic. However, BistaticRCS has a shape dependency, so statistical discussion needs to be done. As the first step in this field, the contour display of BistaticRCS in the focal point of incidence and reflection direction is indicated in Fig. 7. FIG. 7 includes a BistaticRCS for all incident angles relative to the inherent elevation angle.

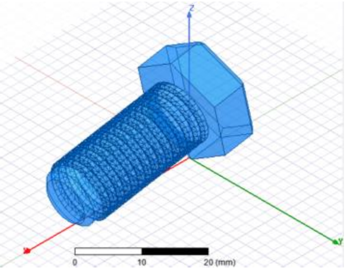

Figure 4. Simulation model for M10 bolt

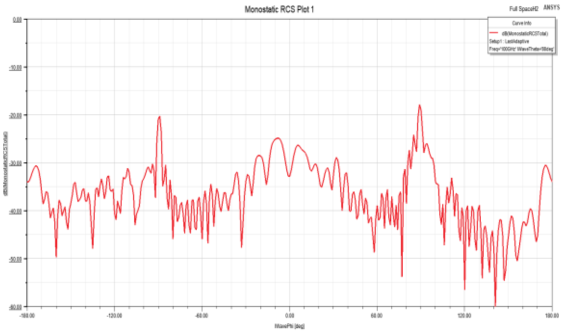

Figure 5. Calculated Monostatic RCS

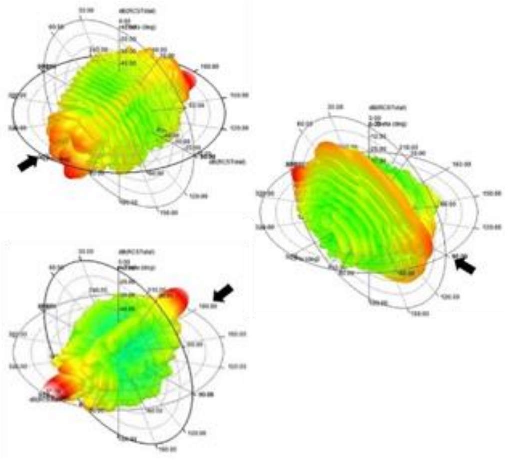

Figure 6. Calculated Bistatic RCS
typical three directions are shown

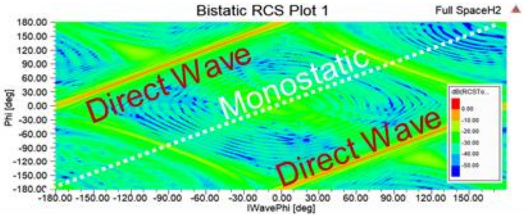

Figure 7. Calculated Contour plot of Bistatic RCS

The plot in FIG. 7 is like a foot-print unique to the object. This pattern is definitely determined by size, shape, and material. In the case of M10 bolt, it is clearly shown that the radar signals are strongly scattered in a specific direction.

5. Conclusion

This paper introduces the outline of the runway foreign object detection system being examined. Recent results of the RCS simulation required for the system evaluation are presented. In order to improve the detection performance of radar, this paper examines a method that calculates RCS at 100GHz. In the future, we will proceed with a statistical evaluation method of detection performance, including the cumulative distribution of RCS.

6. Acknowledgment

This study was conducted as a part of a research project entitled “R&D of a coordinated linear cell radar system in 90GHz-band”, supported by a Japanese Government funding, “ R&D to Expand Radio Frequency resources” of Ministry of Internal Affairs and Communications

References

[1] A. J.Seeds, “Microwave photonics,” IEEE Transaction on Microwave Theory and Techniques, vol.50,pp.877-887,2002 REFERENCES

[2] A. J.Seeds, “Microwave photonics,” IEEE Transaction on Microwave Theory and Techniques, vol.50,pp.877-887,2002

[3] S. Futasumori, A.Kohmura, and N. Yonemoto, ”Performance measurement of compact and high performance 76GHz millimeter-wave system for autonomous unmanned helicopters”, IEICE Technical Report., SANE2011-53, July 2011.

[4] N. Yonemoto, A.Kohmura, S. Futatsumori, T. Ueno, and A. Saillard, ”Broadband RF module of millimeter-wave radar network for airport FOD detection system,” in Proc. Int. Radar Conf.-Surveillance Safer World, Oct. 2009.

[5] A. Kohmura, S. Futatsumori, N. Yonemoto, and K. Okada, ”Optical fiber connected millimeter-wave radar for FOD detection on the runway,” in Proc. 10th Eur. Radar Conf., Oct.2013, pp. 41-44(2013).

[6] S. Futasumori, K. Morioka, A. Kohmura, K. Okada, and N. Yonemoto, ”Evaluation of High-speed FMCW Signal Generation and Processing for Optically-Connected Distributed-Type Millimeter-Wave Radar,” Proceedings of the 2015 International Symposium on Antenna and Propagation(ASAP2015), pp. 903-904, Nov. 2015.

Realtime Remote Sensing of Water/Ice layer on the Runways

Naruto YONEMOTO
Electronic Navigation Research Institute, National Institute of Maritime, Port and Aviation Technology,
182-0012 Chofu, Tokyo, Japan

yonemoto@mpat.go.jp

Abstract –We are investigating the method to detect the presence of water or ice layer on the runway at the airport. We propose a method to use a line laser and a camera. Perpendicular configuration between the laser and camera produces the horizontal shift of the lines according to the thickness of the layer on the ground. The preliminary results indicate the capability to distinguish between water and ice using the scattering of the laser.

Keywords – remote sensing, laser, water/ice layer

1. Introduction

To decrease the occupancy of the runway by landed aircraft, rapid exit taxiways are greatly spread in the world[1]. In the winter airport operations, water or ice on the runway affected the path of the deacceleration of the aircraft. To keep the safe landing, the International Civil Aviation Organization (ICAO) determined the report of the runway condition to the pilot on the landing aircraft[2]. In the regulation, we have to measure the thickness of the contaminant on the runway if the thickness of any kind of contaminant exceeds 3 mm. However, no technology to measure it remotely. Therefore, the airport operation in the early 2020s must rely on human inspection.

Under these conditions, we have started to develop the method to measure the thin layer of water or ice on the runway remotely. In this paper, we tried to develop a new method to measure the thickness of the water/ice layer by laser. The preliminary trials in the laboratory are presented.

2. Realtime runway sensing system

The concept of the runway measurement system is shown in Figure 1. The sensors are located on the side of the runway and rapid exit taxiway where the aircraft moves fast. The lasers make many lines on the surface of the runway. The camera observes the surface and movement of the laser lines if the layer of water or ice appears on the runway. All of the images are transmitted to the monitoring station which is located at quite a far place from the runway. So, we can survey the runway condition not to go to the runway directly.

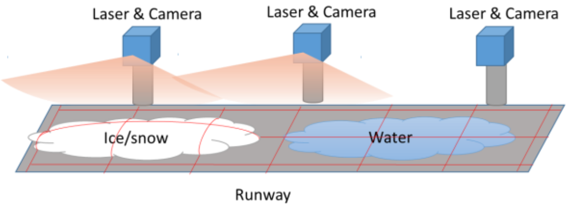

Figure 1. Conceptual figure of realtime remote sensing for runway conditions

3. Laboratory tests

To achieve the detection of the quite thin layer on the runway below 3 mm, we have tried to test many conditions of the line laser and the camera. A typical configuration of the measurement set up is shown in Figure 2. Test samples such as an acrylic plate or measured materials place on the ground plate as the observation area. The laser module placed 1m far from the center of the observation area and 10 cm higher than the ground plate. The images were taken in the various orientation of the camera which is optimized to obtain the larger difference according to the change of the thickness. In our trials, the perpendicular configuration as shown in Figure2 is the best orientation to transfer from the thickness to the horizontal shift of the laser lines.

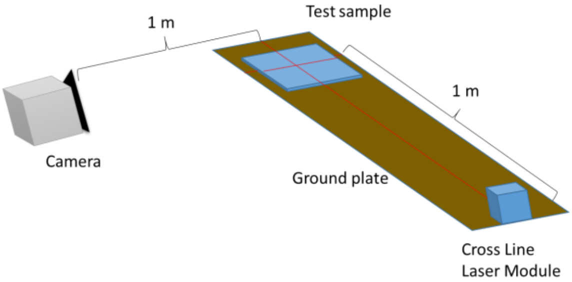

Figure 2. Configuration for the preliminary test

4. Results

Figure 3 shows typical measured results using the solid acrylic plates. The horizontal shift of the laser line is proportional to the thickness of the acrylic plate. 1 mm increase of the thickness is transformed to the 10 mm of the horizontal shift of the laser lines.

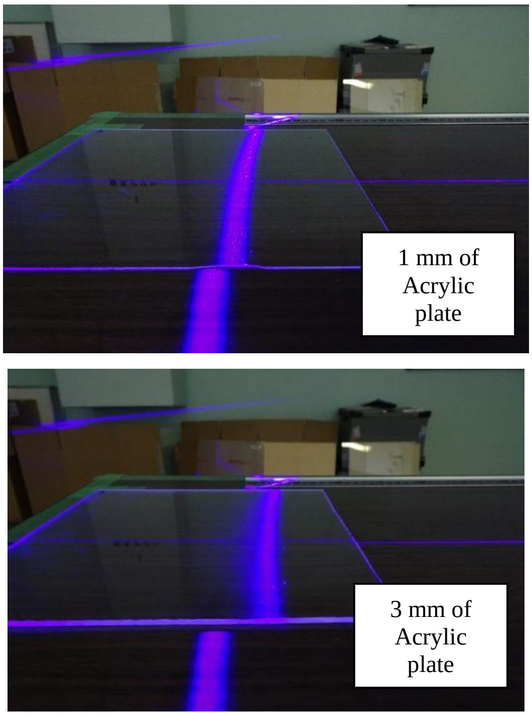

Figure 3. Horizontal shift of lines according to the thickness of acrylic plates

Figure 4 shows the difference between the water and ice layer with 3 mm depth. In the case of the water, several solid lines are observed caused by the reflection on the floor of the palette and surface of the water. In the case of the ice, the broad width of the lines is observed caused by the scattering from the bubbles in the ice. Using pattern recognition, we can discriminate the type of the layer between water or ice with measuring the width of the laser line.

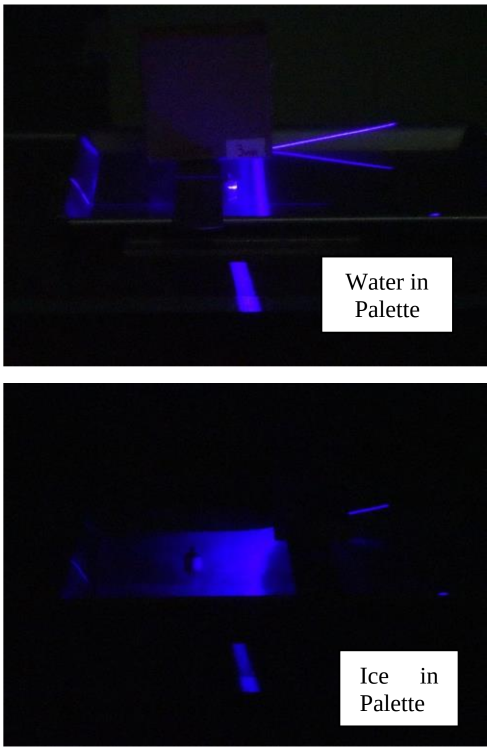

Figure 4. Spread of the light caused by 3 mm depth of the water/ice in the palette.

As a result, we found the laser monitoring method will be applicable for the remote sensing of the growth of the water/ice layer on the runways.

5. Conclusion

We introduced a new method to measure the thickness of the thin water/ice layer. We will improve the focus of the laser to increase the resolution of the system and will develop the invisible system using infrared devices for the airport operations as the future work.

References

[1] ICAO International Standards and Recommended Practices, Annex 14 to the Convention on International Civil Aviation, “Aerodromes”, Volume 1, Eighth Edition, July 2018

[2] ICAO, Doc.9981, Procedures for Air Navigation Services, Aerodromes, Second Edition, 2016

Progress and Prospects of THz Time-Domain Imaging for Nondestructive Testing

Case Studies on Cultural Heritage in 10 Years

Kaori FUKUNAGA[1*]
[1]Electromagnetic Applications Laboratory, NICT, 184-8795 Tokyo, Japan
*kaori@nict.go.jp

Abstract – The advantage of the use of electromagnetic waves in nondestructive test is that its imaging technology can provide internal structure of opaque objects without contact. We have been applied to THz time domain imaging to examination of paintings and revealed techniques of artists and previous conservators. By using multiple devices from microwave to near infrared, it is possible to examine wide range of heritage objects from ancient mural paintings to contemporary plastic artworks.

Keywords – terahertz; time-domain; imaging; heritage science

1. Introduction

In general nondestructive tests, the most commonly used electromagnetic technique is the X-ray radiography, and eddy current comes the second. Even microwave, which is considered to be a mature technology, has been only used for underground radars in the limited field of civil engineering. The reason could be that large structural parts are made of metals, and ultrasonic waves and thermography have been sufficient for the inspection. In addition, nondestructive inspection technology itself is categorised in one field of mechanical engineering, which may cause the lack of radio wave specialists. In the present day, however, reinforced plastics and their composite materials have come to be used for infrastructures, and thus the importance of nondestructive inspection using electromagnetic waves will increase.

The advantage of using electromagnetic waves in nondestructive test is that the technique can provide internal structure of opaque objects without contact. Except ionizing radiation, such as X-ray radiography, when the frequency is high, the spatial resolution is high, but the penetration depth becomes short from the surface. In these 20 years, terahertz (THz) time domain imaging technology has been actively developed and has been applied to examine coatings of various objects, including radomes and oil tanks.

We have been applied to THz time domain imaging to cultural heritage objects, and proved that THz frequency range is particularly useful for observing the preparation layer of painting that cannot be observed by other nondestructive measures. In this talk, practical applications of THz time domain imaging are introduce by showing case studies on masterpieces in these ten years, and future prospects are discussed.

2. Electromagnetic waves used in nondestructive test

Figure 1 introduces the use of electromagnetic waves from microwave to X-ray for internal structure observation, with some examples obtained in our previous works. Here material identification and/or spectroscopic imaging are not mentioned in this talk, because there are various established methods that give sufficient information to conservators and historians [1, 2]. Figure 2 shows typical painting layer structures and applicable frequency range to observe their interfaces. The oldest Paleolithic mural paintings, such as those in Chauvet Cave are still clear because they were painted in the limestone caves with mineral colours, although we do not know it was intentional or not. At the latest, in 6000 BC, humans created mortar layer, and particular mineral pigments were used to paint. This leads to the current fresco technique established in the 1300s, of which cross section is described in Fig. 2 (a). Microwaves are necessary to observe the support, and mm-wave and THz can be applied to observe preparation layers. X-ray transmission can be used only for fragments. In general, the fresco technique does not use binders, and colours are covered by chemical reactions that generate calcite layer on the surface. On the other hand, painting technique with binders can be applied to any types of support without mortar layers. There are various techniques from Egyptian mummies to modern acrylic paintings. The thickness of preparation layers indicated in Fig. 2 (b) depends on the technique and varies from sub-micron to several hundred microns. If the work is small, the internal structure can be observed by X-ray CT, but THz is particularly effective for the restoration staff because they want to know the support and the underlying layer.

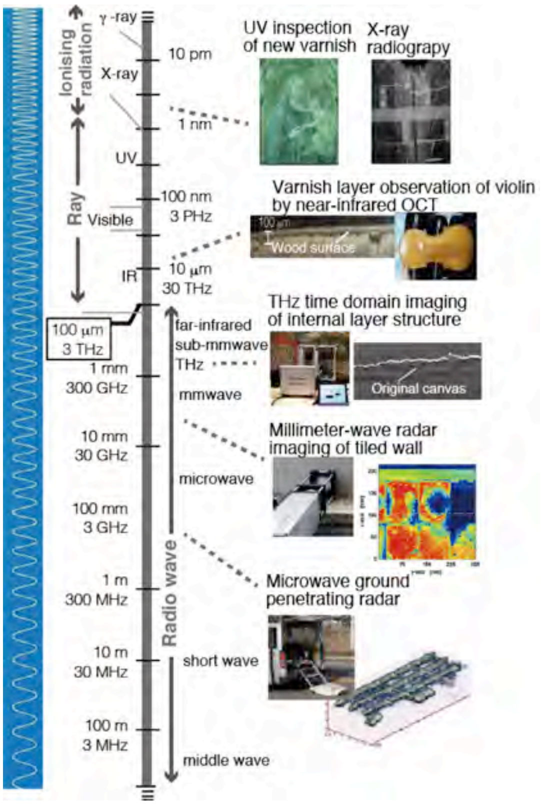

Figure 1. Electromagnetic waves used in nondestructive tests.

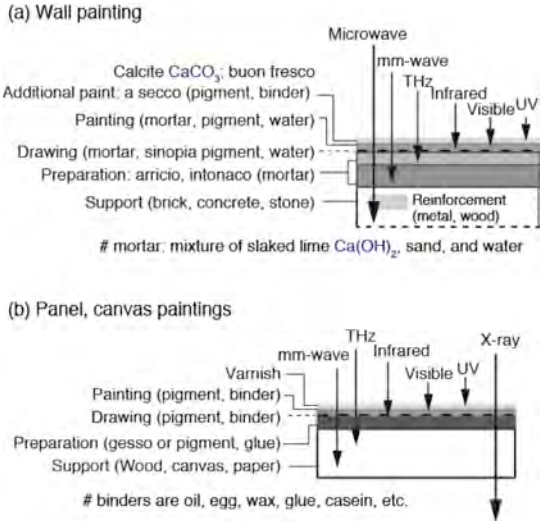

Figure 2. Penetration depth depends on frequency range.

While THz technology is not yet commonly used in most industries, the THz time-domain imaging technique has been adopted in heritage science, because it non-destructively reveals the internal layer structure from support to painted surface that is the most important part for conservation treatment. Details of the THz time-domain technology are precisely introduced in many review articles including a recent milestone article of THz imaging by D. M. Mittleman [3].

3. Examples of THz imaging applied to cultural heritage

THz imaging technique has been applied to various museum objects, and some examples carried out by NICT are shown in Fig. 3, along the chronological table of art history [4]. The first application was performed in 2008, during the conservation of "Polittico di Badia" (1300), a masterpiece of Giotto, at the Uffizi Gallery. The non-destructive cross-section image clearly showed that two gesso layers exist in the panel, which proved that the artist followed the medieval technique. The "Cypress Tree" on Tokyo National Museum is a panel screen, which was under conservation from 2012 to 2014. THz imaging revealed many pieces of mending paper below the painting, which give the history of the artwork, as well as useful information for treatment planning.

Among these examples, up to now, there are two unsolved issues. One is the original painting technique of Bernt Notke's canvas painting "Danse Macabre" (15th century) in the Niguliste Museum in Estonia. Some parts seem to have two painting layers. A conservation scientist suggested that the technique might be the glue-sized, which uses animal glue and pieces of thin fabric to paint. Further investigation is required to interpret the experimental results. Another issue is over-paint layers of “Homme au Chapeau” (1915), by Pablo Picasso, in the Tokyo Station Gallery [4]. The layer structure of the painting depends on the area. By extracting the second layer, the image becomes similar to a photograph shown in a catalogue [5], which is rather different from current image introduced in another catalogue and a book [6]. Art historians' viewpoints are required to understand these results.

4. Possible contribution to emerging issue in heritage science

Recently we found that THz time-domain imaging is effective for a specific problem that has been one of the emerging issues in conservation of canvas paintings, during the measurement of "Venus and sailor (Homage to Salvat-Papasseit, 1925, 215 × 147.5 cm)" by Salvador Dalí (1904–1989)" [7]. According to the artist himself, it was painted many times on another old painting acquired by his father. First, Dalí made an impressionist painting on it, then friends' portraits, then another subject with tempera, and finally it has become "Venus and sailor". Moreover, several intervention treatments were carried out on this painting in the 20th century. The back of the original canvas may have been lined with linen sheets that were glued with wax, then finally tightly glued to an aluminium panel with wax [8]. This type of "wax-conservation" was developed, patented and used mainly in the US, resulting in serious problems. Indeed,

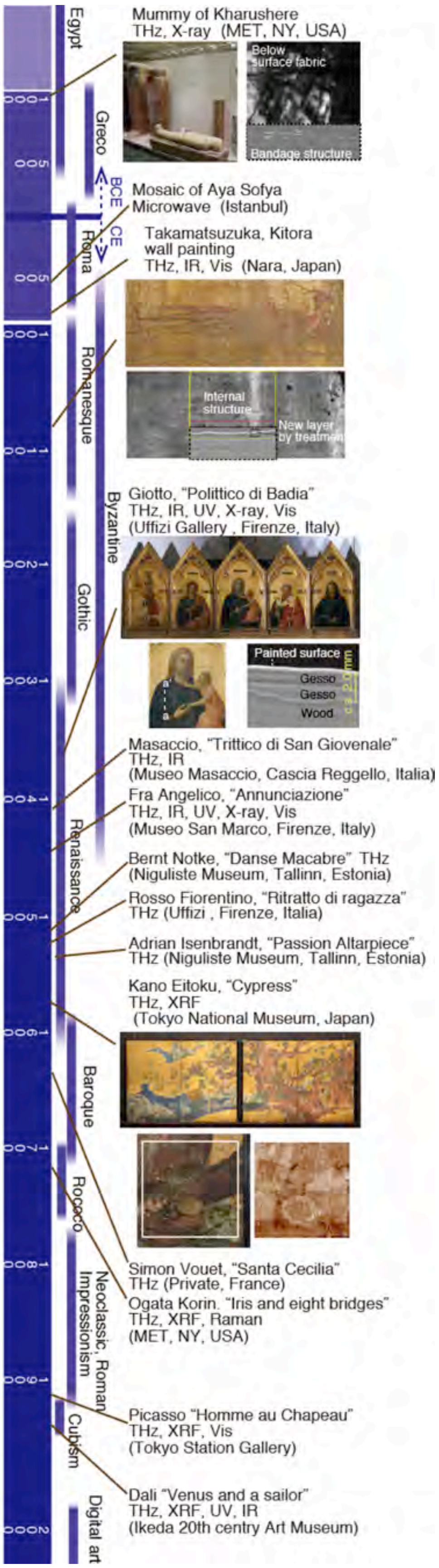

Figure 3. Artworks investigated by NICT.

the removal method is an emerging issue in heritage science [9].

Figure 4 shows a typical cross section image of this painting, and output signals at the points A and B indicated in the image. In both signals, the first reflection peak is generated at the painting surface, and the last peak is from the aluminium plate that was used for conservation purposes by a previous conservator. The peaks appeared between these two are generated by internal interfaces. Since the refractive index of each layer depends on the material, the velocity of the THz wave is different in each painted layer. Although the exact thickness of each layer cannot be obtained without knowing the precise material properties, qualitative characteristics including the number of layers can suggest the history of this painting. The reflection signals from the aluminium support clearly appear as a white line at the bottom of the cross section image. Then, there is a thick uniform layer, which could be composed of three internal layers. Judging from the edge of this layer and the literature on wax treatment, this bottom uniform layer is deduced to be a lining layer composed of linen fabric sheets and wax.

On the other hand, multiple layers near the surface, which appear in most part of the painting, are considered to be "painted" layers. This structure agrees with the artist's comments. On the right end, however, a thick single paint layer exists. As the delay of the reflection signal from the lining layer is much larger in other areas, the unknown material should have a larger refractive index. Such internal structure observation can provide useful information for future conservation planning.

To conclude, it is important for users to select the appropriate frequency band according to the object to be measured. Hopefully, more electromagnetics and optics experts join nondestructive inspection research fields, especially in heritage science.

Finally, the author acknowledges conservators, curators and art historians for their fruitful discussions.

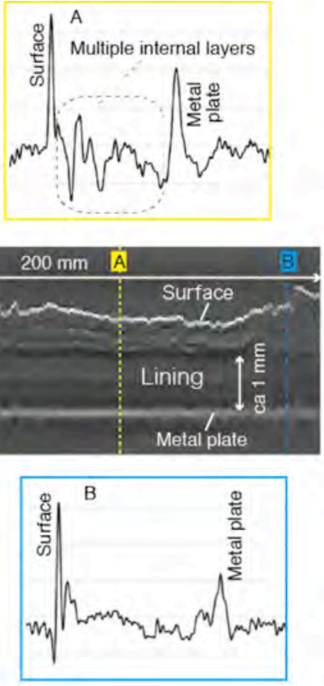

Figure 4. Example of cross section image of a part of "Venus and sailor", by Salvador Dalí.

References

[1] Masini N, Soldovieri F, Eds., *Sensing the Past*, Springer; 2017.

[2] Delaney JK, et al, "Visible and infrared imaging spectroscopy of paintings and improved reflectography", Heritage Science, 2016; DOI: 10.1186/s40494-016-0075-4.

[3] Mittleman DM, Twenty years of terahertz imaging, Optics Express, 2018; 26: 9417-9431.

[4] Fukunaga K, THz Technology Applied to Cultural Heritage in Practice, Springer; 2016.

[5] Daix P, J. Rosselet, Le Cubisme de Picasso, Editions Ides et Calendes, Neuchâtel; 1979.

[6] Richardson J, A Life of Picasso, Jonathan Cape, London; 1996.

[7] Fukunaga K, et al, Nondestructive observation of multilayered modern paintings by electromagnetic waves, Proc. SPIE 11058, Optics for Arts, Architecture and Archaeology VII, 2019, No. 1105802.

[8] Mecklenburg MF, et al.,"Honeycomb Supports: Their Fabrication and Use in Painting Conservation", Studies in Conservation, 1977; 22(4); 177-189

[9] Books C, et al., "The lining of canvas onto aluminum sheet interleafs: History and approaches for their reversal", AIC's 47th Annual Meeting, 2019, No. 19110

Characterisation of Terahertz Antenna for beyond 5G Systems

Akihiko Hirata[1*] , Katsumi Fujii[2], N. Sekine[2], I. Watanabe[2], A. Kasamatsu[2]
[1]Faculty of Engineering, Chiba Institute of Technology, 275-0016, Narashino-shi, Chiba, Japan
[2] National Institute of Information and Communications Technology, 184-8795, Koganei-shi, Tokyo, Japan
*Corresponding author: hirata.akihiko@p.chibakoudai.jp

Abstract – It is important to build the antenna and propagation models of THz wireless communications in order to evaluate the interference between other services, and to estimate communication quality of THz wireless communications. ThoR (TeraHertz end-to-end wireless systems supporting ultra-high data Rate applications) project is a joint EU-Japan project to provide technical solutions for the data networks beyond 5G based on 300 GHz RF wireless links. This paper presents the measurement results of 300-GHz-band antenna and propagation characteristics in ThoR project.

Keywords – terahertz; antenna; propagation; beyond 5G;

1. Introduction

Terahertz (THz) wireless systems are a very promising solution for beyond 5G system [1]. World Radiocommunication Conference (WRC) 2019 will be held in Oct-Nov 2019, and its agenda item 1.15 relates to consideration of identification of frequency bands for the land-mobile and fixed services applications operating at 275-450 GH [2].

It is important to evaluate the antenna pattern in order to evaluate the communication quality of THz wireless system, or in order to avoid the interference between backhauls and fronthauls or with these passive services. There are passive services, such as earth exploration-satellite service (EESS), operating in this frequency range, and sharing between THz wireless links and EESS will be discussed at WRC 2019.

One of the important parameters for evaluation of the interference between different systems is the radiation pattern of antennas. International Telecommunication Union Radiocommunication Sector (ITU-R) defines the antenna pattern models in Recommendation ITU-R F.699 and F.1245 [3]. However, these Recommendations cover at a frequency range of up to 87 GHz, and there are no recommendations that defines the radiation pattern of antennas at a frequency range of over 100 GHz. It is difficult to measure accurate radiation patterns at THz frequency range, because the output power of THz transmitter and the sensitivity of THz receiver is not so high, which makes the measurement system dynamic range small.

ThoR (TeraHertz end-to-end wireless systems supporting ultra-high data Rate applications) project is a joint EU-Japan project to provide technical solutions for the data networks beyond 5G based on 300 GHz RF wireless links [4]. One of the objective of this project is the experimental characterization of 300 GHz antennas and to build antenna model at THz range. This paper presents the overview of ThoR project and the measurement results of THz antenna and propagation characteristics.

2. Overview of ThoR project

The ever-increasing demand for higher data transfer rates in up- and down-link for each device in a mobile network leads to huge aggregated data rates, especially in cities [5]. To service a fully mobile and connected society networks beyond 5G system must undergo tremendous growth in connectivity, data traffic density and volume as well as the required multi-level ultra-densification. The ThoR project is a joint EU-Japan project and started July 2018. Figure 1 shows an overview of ThoR project [4]. ThoR will apply state-of-the-art photonic and electronic technologies to

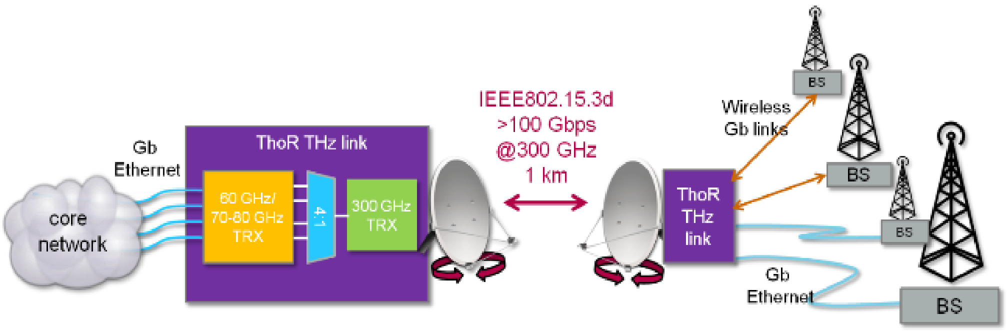

Figure 1. Overview of ThoR project [4].

build an ultra-high bandwidth, high dynamic range transceiver operating at 300 GHz combined with state-of-the-art digital signal processing units, and final objective is >100 Gbps P2P link at 300 GHz.

One of the objective is the characterization of the antenna and propagation environment and produce advisory documents, which will be fed into international standardization conferences. Figure 2 shows the antenna and propagation studies in ThoR project. The objectives of this activities are (a) to make an antenna model in the 275-325 GHz region, (b) to derive THz propagation models, (c) interference studies with passive services, and (d) to make the base station deployment scenario for space division multiplexing of backhaul/fronthaul links.

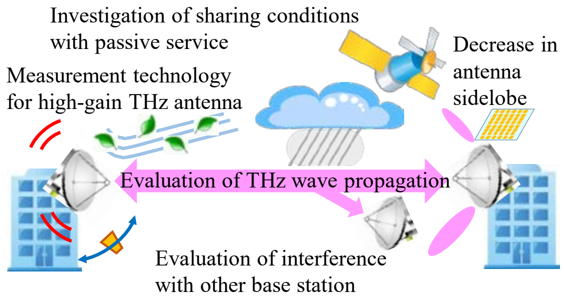

Figure 2. Antenna and propagation studies in ThoR project [4].

3. Antenna pattern measurement

WRC 2019 will be held in Oct-Nov 2019, and identification of frequency bands for the land-mobile and fixed services applications operating at 275-450 GH will be discussed. One of the main issues in the conference is frequency sharing between THz wireless service and EESS. In order to evaluate the interference from THz wireless service to EESS, the accurate antenna model is necessary. However, there is no ITU-R model of radiation pattern that covers up to 300 GHz. Therefore, the sharing studies on Agenda Item 1.15 employs the existing Recommendation ITU-R F.699 and F.1245 that covers up to 87 GHz. Moreover, the experimental characterization data of high-gain antenna at THz range is few [6]. It is difficult to measure accurate antenna patterns at THz frequency range. The output power of THz transmitter and the sensitivity of THz receiver is not so high because of the limitation of semiconductor devices at these frequency range. Therefore, the dynamic range of radiation pattern measurement system at THz range is smaller than that at microwave range and millimeter-wave range. The narrow dynamic range of measurement system makes it difficult to obtain accurate sidelobe pattern of high gain antenna, because the power ratio of sidelobe is much smaller than that of main lobe. The antenna pattern should be measured at far field. In case the antenna gain is 45 dBi (antenna diameter: 0.15 m) and the frequency is 300 GHz, the boundary of far field is 45 m. In this case, the free-space propagation loss (FSPL) is about 115 dB, and the received power is quite small, especially in case of the measurement of side lobe pattern.

Figure 3 shows the measurement results of a low-gain antenna (WR-3.4 standard horn antenna). In order to achieve accurate radiation pattern measurement of this antenna, we employed a vector network analyser (VNA) and the measurement was conducted in a small anechoic chambers at

NICT. Two horn antennas were opposed to each other at a distance of 0.5 m. The measured radiation pattern agreed well with the simulation results.

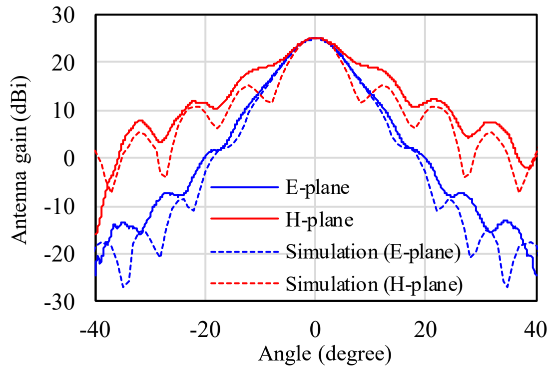

Figure 3. Radiation patterns of WR-3.4 standard horn antenna at 300 GHz.

We also measured the radiation pattern of a high-gain Cassegrain antenna with a diameter of 150 mm (45 dBi). The experimental results are shown in Figs. 4. The antenna pattern models described in Recommendation ITU-R F.699-8 and F1245-3 are also shown. A small dip was observed at the top of the main lobe. In this experiment, the transmission distance was 20 m. This distance is smaller than the boundary of far field (45 m). Therefore, the shadowing effect of the secondary reflector are observed. The sidelobes of measured radiation patterns are larger than that of ITU-R antenna pattern models. These results indicate that new antenna pattern models at 300-GHz band are necessary. In order to measure the accurate radiation pattern of the Cassegrain antenna, we have to increase the transmission distance. It is difficult to set the transmission distance over 45 m in an anechoic chamber. We are going to make a transmitter and to obtain an experimental radio station license. By using this transmitter, we are going to conduct outdoor transmission experiments. Another way to obtain an accurate radiation pattern of the high-gain antenna is the conversion of measured near-field pattern to far-field pattern. Near field measurement of high-gain antenna by EO probe is one of the promising solution [7].

As shown in Fig. 2, it is important to suppress sidelobes of high-gain antennas. We are now investigating a 300-GHz-band THz absorber that employs surface metamaterials. The THz absorber employs slot ring resonator (SRR) absorber [8] that is shown in Fig. 5(a). The SRR patterns are made by a 2-μm-thick gold on a 200-μm-thick quartz substrate. The simulation results of S_{21} is shown in Fig. 5(b). S_{21} at 296.7 GHz is -32.4 dB, and -10-dB bandwidth is about 37.7 GHz. We are planning to use these THz absorber to suppress the sidelobes of THz high-gain antenna.

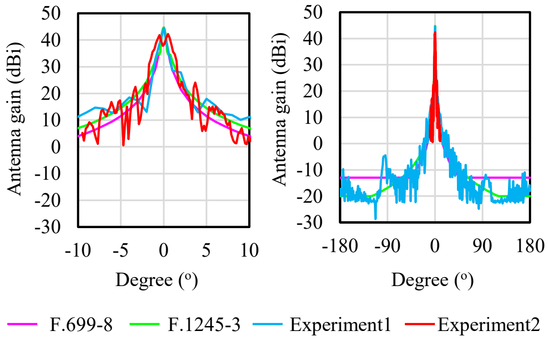

Figure 4. Radiation patterns of Cassegrain antenna at 300 GHz, and that of Recommendation ITU-R.

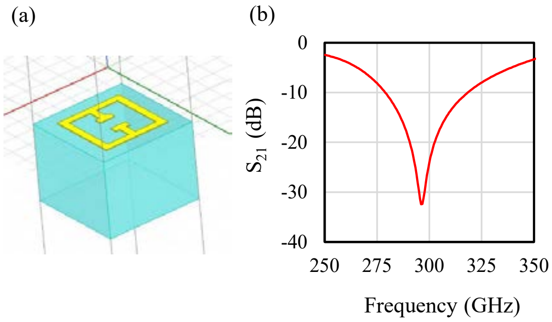

Figures 5. (a) Unit cell of THz absorber. (b) Simulation result of transmission characteristics of THz absorber.

4. Reflection characteristics of building materials

To increase the accuracy of radio wave propagation simulation, accurate material property model, such as reflection coefficient of building materials, should be used. Material property models described in Recommendations IUT-R P.1238 and P.2040 are usually used for the propagation simulations [9]. However, there is no recommendation of material property models that can be used for the 300-GHz-band THz wave propagations. We measured the reflection characteristics of various building materials on the incident angle. We used two diagonal horn antennas with a gain of 25 dBi, and they are attached with the frequency extenders for the VNA. Figure 6 shows the dependence of reflection characteristics of wood and glass on the incident angle. Periodic fluctuations are observed. These periodic fluctuations come from the superposition of reflection wave at the sample surface and at the sample bottom. As the incident angle increases, S_{21} increases. The period of the fluctuations becomes shorter as the incident angle decreases. We conducted outdoor propagation simulations using these measured reflection characteristics in order to evaluate the interference between fronthaul wireless links that are placed nearby each other. We are going to measure the complex permittivity of building materials by using terahertz time domain spectroscopy (THz-TDS) [10].

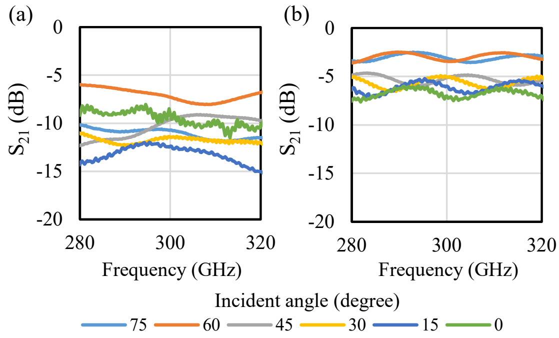

Figures 6. Reflection characteristics of (a) wood and (b) glass at 280-320 GHz.

5. Conclusion

We conducted the measurement of 300-GHz-band antenna and propagation characteristics in ThoR project. Radiation pattern measurement of high-gain THz antenna is difficult due to the limitation of measurement equipment dynamic range and that of transmission distance of propagation experiment. The sidelobe pattern of high-gain antenna did not coincide with the antenna model described in Recommendation ITU-R. These results indicate we have to evaluate the accurate radiation pattern of high-gain antenna at 300 GHz, and make new antenna model at this frequency. The conversion of measured near-field pattern by EO probe to far-field pattern is one of the promising solution to obtain an accurate radiation pattern of the high-gain antenna. Measurement of reflection characteristics of building materials is important to evaluate the interference between fronthaul wireless links that are placed nearby each other.

ACKNOWLEDGMENT

Part of this work is supported in part by Japan-EU Joint Program of National Institute of Information and Communications (NICT), and MEXT KAKENHI Grant Number JP 17H03268.

References

[1] H. Elayan, O. Amin, R. M. Shubair, and M.-S. Alouini, Terahertz Communication: The Opportunities of Wireless Technology Beyond 5G. 2018 International Conference on Advanced Communication Technologies and Networking (CommNet), 2-4 April 2018, Marrakech, Morocco, 1570443178.

[2] https://www.transfinite.com/content/wrc2019-17

[3] https://www.itu.int/rec/R-REC-F/en

[4] https://thorproject.eu/

[5] J. J. H. Wang, Broadband-Multiband Antennas Enabling Capacity & Security for Mobile Wireless 5G and Beyond. 2018 International Symposium on Antennas and Propagation (ISAP) 23-26 Oct. 2018, Busan, Korea, WeA2-1.

[6] X. Xu, X. Zhang, Z. Zhou, T. Gao, Q. Zhang, Y. Lin, and L. Sun, Terahertz Cassegrain Reflector Antenna. 2013 International Symposium on Antennas & Propagation, 23-25 Oct. 2013, Nanjing, China, pp. 969-972.

[7] H. Huy N. Pham, S. Hisatake, and T. Nagatsuma Far-field antenna characterization in the sub-THz region based on electrooptic near-field measurements. 2014 International Topical Meeting on Microwave Photonics (MWP), 20-23 Oct. 2014, Hokkaido, Japan, WC-7.

[8] K. Itakura, A. Hirata, M. Sonoda, T. Higashimoto, T. Nagatsuma, T. Tomura, J. Hirokawa, N. Sekine, I. Watanabe, A. Kasamatsu, Investigation of plasmon hybridization between slot-ring resonator absorber and lattice pattern substrate 2019 International Symposium on Antennas & Propagation, 27-30 Oct. 2019, Xi’an, China.

[9] https://www.itu.int/rec/R-REC-P/en

[10] H. Igawa, T. Mori, S. Kojima, Terahertz time-domain spectroscopy of congruent LiNbO3 and LiTaO3 crystals. Japanese Journal of Applied Physics, Vol. 53, No. 5S1. 05FE01. 2014.

THz dual-comb spectroscopy using a free-running single-cavity wavelength-multiplexed mode-locked fiber laser

Takeshi Yasui[1,2]
[1] Institute of Post-LED Photonics, Tokushima University, Tokushima 770-0813, Japan
[2] JST, ERATO MINOSHIMA Intelligent Optical Synthesizer (IOS), Tokushima, Japan
*Corresponding author: yasui.takeshi@tokushima-u.ac.jp

Abstract – Terahertz dual-comb spectroscopy (THz-DCS) enables high spectral resolution, high spectral accuracy, and broad spectral coverage; however, the requirement for dual stabilized femtosecond lasers hampers its versatility. We here demonstrate THz-DCS using a free-running single-cavity wavelength-multiplexed mode-locked fiber laser. By multiplexing the mode-locking oscillation in wavelength region, dual-wavelength comb light beams with slightly detuned repetition frequencies are generated in a single laser cavity. Due to sharing of the same cavity, such comb light beams suffer from common-mode fluctuation of the repetition frequency, and hence the corresponding frequency difference between them is passively stable. The demonstrated results indicate that this system is an attractive solution for practical applications of THz spectroscopy and other applications.

Keywords – terahertz; optical comb; dual-comb spectroscopy; gas spectroscopy

1. Introduction

Since many materials indicate spectral fingerprints in the terahertz (THz) region (freq. = 0.1~10 THz), THz spectroscopy has attracted great research interests. In contrast to the traditional THz time-domain spectroscopy, THz dual-comb spectroscopy (THz-DCS) could potentially measure broad THz spectrum with high resolution and moderate acquisition speed [1]. Besides, its absolute accuracy can be traceable to the Rubidium frequency standard [2]. However, this system requires a pair of two stabilized comb lasers for generation and detection of THz comb. Although the requirement for the frequency stabilization can be cancelled by help of adaptive sampling technique [3], a pair of comb lasers is still required. The associated cost and system complexity hinder the wider application of THz-DCS technique. Recently, multiplexed mode-locked fiber lasers based on wavelength-multiplexing, polarization-multiplexing, bidirectional lasing or intracavity nonlinear pulse shaping [4-7] have emerged as a choice of dual-comb sources with low common mode noise [8, 9], and been successfully applied to the asynchronous optical sampling [10, 11], frequency metrology in the microwave [12] and THz region [8], and optical spectroscopy [9].

In this paper, by tailoring the intracavity dispersion, wavelength-multiplexed mode-locked fiber laser with low repetition-rate-difference (Δf_{rep}) is realized to enable sufficient temporal magnification in the asynchronous optical sampling. Without any stabilization, such a fiber laser is effectively applied to a THz-DCS system [13].

2. Experimnental setup

THz-DCS consists of the wavelength-multiplexed mode-locked fiber laser (λ_1 = 1531nm, λ_2 = 1543nm; P_1 = 20mw, P_2 = 27mW, $\tau_1 = \tau_2$ = 130fs; $f_{rep1} \approx f_{rep2} \approx$ 64.55 MHz, $\Delta f_{rep} \approx$ 245 Hz), a cross-correlation signal generator for the trigger generation, two fiber-coupled InGaAs PCAs as the emitter and detector of THz pulse, and the data acquisition electronics. The emitted THz pulse was generated from the PCA emitter triggered by the λ_1 pump light, propagated in free space, and then was incident onto the PCA detector together with the λ_2 probe light. Then the generated electrical signal from the PCA detector was acquired by the fast digitizer after amplified by a current amplifier. For comparison, two commercialized frequency-stabilized fiber lasers ($\lambda_1 \approx \lambda_2 \approx$ 1550nm; $P_1 = P_2$ = 20mW, $\tau_1 = \tau_2$ = 50fs; $f_{rep1} \approx f_{rep2} \approx$ 250MHz, $\Delta f_{rep} \approx$ 893Hz) that provide the same time magnification factor are used in the same THz-DCS setup, and their performance are compared to each other.

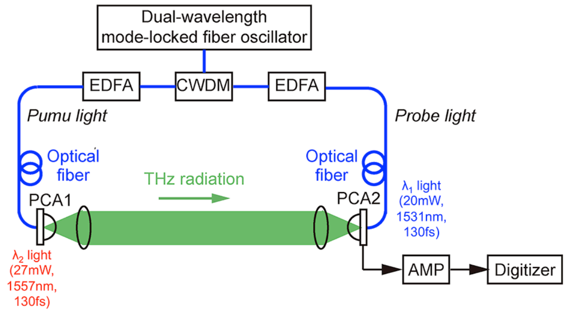

Fig. 1. Experimental setup.

3. Results

Figure 2(a) shows the comparison of THz power and noise spectra between the present THz-DCS system using the dual-λ-ML fiber laser and previous THz-DCS system using two stabilized lasers. The spectral bandwidth was comparable to each other.

We next evaluated dynamic range of spectral power at 0.2~0.4 THz with respect to the data acquisition time for both systems as shown in Fig. 2(b), showing the similar linear slope. Also, the slopes of them are overlapped, indicating comparable DR characteristic to each other. In this way, the present system shows the comparable performance to the present system in the spectral bandwidth and dynamic range even though dual stabilized lasers are not used.

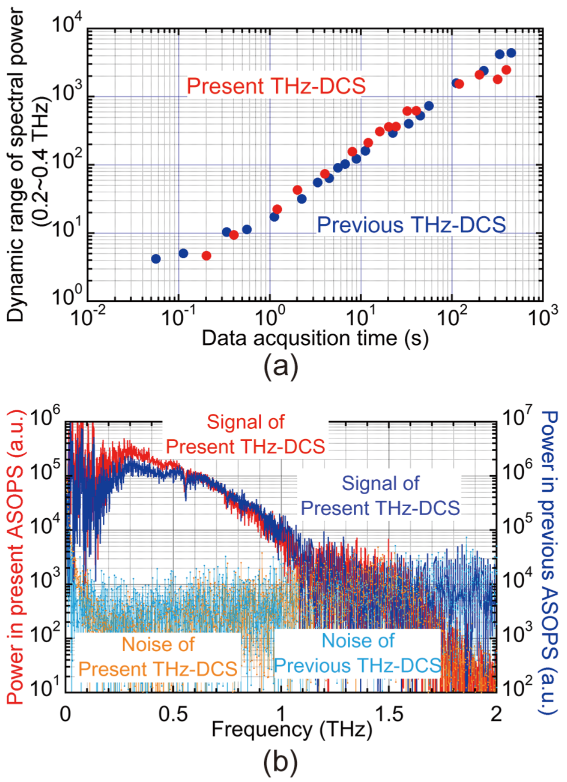

Fig. 2. Basic performance. (a) Power and noise spectra and (a) dynamic range of spectral power for present and previous ASOPS-THz-TDS systems.

Finally, we demonstrated THz spectroscopy of acetonitrile (CH_3CN) gas under atmospheric pressure. Since CH_3CN gas is contained in the interstellar medium, incomplete combustion gas of nylon textiles, volatile organic compounds related with atmospheric pollution and biomarkers, it is important to perform THz spectroscopy of this molecular gas in astronomy, fire accidents, atmospheric analysis, and health monitoring. Due to the symmetric top molecule, CH_3CN gas exhibits characteristic spectral fingerprints with GHz structure in the THz region under atmospheric pressure: a series of manifolds of multiple rotational transitions regularly spaced by 2B, where B is the rotational constant (= 9.194 GHz). After an enclosed box for THz optics was filled with CH_3CN gas at atmospheric pressure, the THz power spectrum was acquired by the present THz-DCS system. Figure 3 shows the absorbance spectrum of CH_3CN gas (data acquisition time = 257 s). Thirty-nine manifolds of absorption lines periodically appeared with a constant frequency separation, and could be assigned to rotational quantum numbers from J=15 around 0.29 THz to J=53 around 0.98 THz correctly.

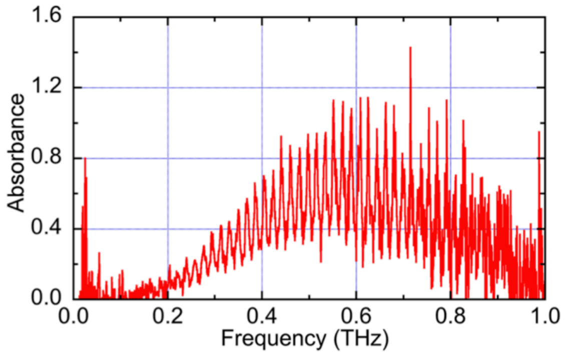

Fig. 1. Spectroscopy of CH_3CN gas.

4. Summary

THz-DCS with a free-running dual-λ-ML fiber laser has the great potential for low complexity, cost-effective and portable, high-performance spectrometer.

This work was supported by JST, ERATO MINOSHIMA Intelligent Optical Synthesizer (IOS).

References

[1] T. Yasui *et al.*, "Terahertz frequency comb by multi frequency-heterodyning photoconductive detection for high-accuracy, high-resolution terahertz spectroscopy," Appl. Phys. Lett. **88**, 241104 (2006).

[2] Y. D. Hsieh *et al.*, "Terahertz comb spectroscopy traceable to microwave frequency standard," IEEE Trans. Terahertz Sci. Tech. **3**, 322-330 (2013).

[3] T. Yasui *et al.*, "Adaptive sampling dual terahertz comb spectroscopy using dual free-running femtosecond lasers," Sci. Rep. **5**, 10786 (2015).

[4] X. Zhao *et al.*, "Switchable, dual-wavelength passively mode-locked ultrafast fiber laser based on a single-wall carbon nanotube mode locker and intracavity loss tuning," Opt. Express **19**, 1168-1173 (2011).

[5] X. Zhao *et al.*, "Coherent dual-comb mode-locked fiber laser based on a birefringent ring cavity," in *Frontiers in Optics 2015*, FW3C.3.

[6] X. Zhao *et al.*, "Dual-wavelength, bidirectional single-wall carbon nanotube mode-locked fiber laser," IEEE Photon. Technol. Lett. **26**, 1722-1725 (2014).

[7] Y. Liu *et al.*, "Unidirectional, dual-comb lasing under multiple pulse formation mechanisms in a passively mode-locked fiber ring laser," Opt. Express **24**, 21392-21398 (2016).

[8] G. Hu *et al.*, "Measurement of absolute frequency of continuous-wave terahertz radiation in real time using a free-running, dual-wavelength mode-locked, erbium-doped fibre laser," Sci. Rep. **7**, 42082 (2017).

[9] X. Zhao *et al.*, "Picometer-resolution dual-comb spectroscopy with a free-running fiber laser," Opt. Express **24**, 21833-21845 (2016).

[10] X. Zhao *et al.*, "Fast, long-scan-range pump-probe measurement based on asynchronous sampling using a dual-wavelength mode-locked fiber laser," Opt. Express **20**, 25584-22589 (2012).

[11] X. Zhao *et al.*, "Coherent asynchronous sampling distance measurement using a single polarization-multiplexed ultrafast laser," in *Conference on Lasers and Electro-optics 2014*, STh4O.2.

[12] X. Zhao *et al.*, "Dead-band-free, high-resolution microwave frequency measurement using a free-running triple-comb fiber laser," IEEE J. Sel. Topics Quantum Electron. **24**, 1101008 (2018).

[13] G. Hu *et al.*, "Dual terahertz comb spectroscopy with a single free-running fibre laser," Sci. Rep. **8**, 11155 (2018).

Optical Frequency Comb Techniques for mm-wave Radio over Fibre and THz over Fibre

G.K.M. HASANUZZAMAN*, and Stavros IEZEKIEL
Department of Electrical and Computer Engineering, University of Cyprus, 1678, Nicosia, Cyprus
*Corresponding author: ghasan01@ucy.ac.cy

Abstract – We demonstrate two driving scenarios for an optical frequency comb generator (OFCG), namely an OFCG driven by an optoelectronic oscillator (OEO) driven, and a self-oscillating version. These are then applied to mm-wave generation and radio over fiber (RoF) links. In the OEO driving structure, the electrical output of an OEO drives the OFCG while in the self-oscillating topology the oscillating loop also functions as an OFCG. With the combination of two-tone selection and optical heterodyning, mm-wave and THz signals are generated. We implemented a RoF link based on a self-oscillating OFCG where the modulating signal was a standard LTE-A signal with 64 QAM modulation format and EVM lower than the EVM limit.

Keywords – radio-over-fiber, optical frequency comb generator, optoelectronic oscillator, microwave photonics

1. Introduction

The integration of the optical frequency comb generator (OFCG) and optoelectronic oscillator (OEO), either in a self-oscillating mode or as a separately driven architecture is a promising concept for mm-wave and THz signal generation, and further implementation in a radio over fibre link [1],[2]. The conceptual block diagrams of an OFCG, OEO, OEO-driven OFCG, and self-oscillating OFCG are shown in Fig.1. An OFCG can provide evenly spaced discrete optical multi-tones as shown in Fig. 1(a) and a conventional optical modulation based comb generator is driven by an external RF source which determines the comb spacing. An OEO is a hybrid oscillator which can yield pure oscillation either in the microwave domain or microwave modulated optical domain as shown in Fig. 1(b) [3]. The integration of an OFCG and OEO is shown in Fig. 1(c), in which the OEO drives the OFCG, in Fig. 1(d) a self-oscillating version is depicted in which the OFCG is embedded directly into the OEO loop.

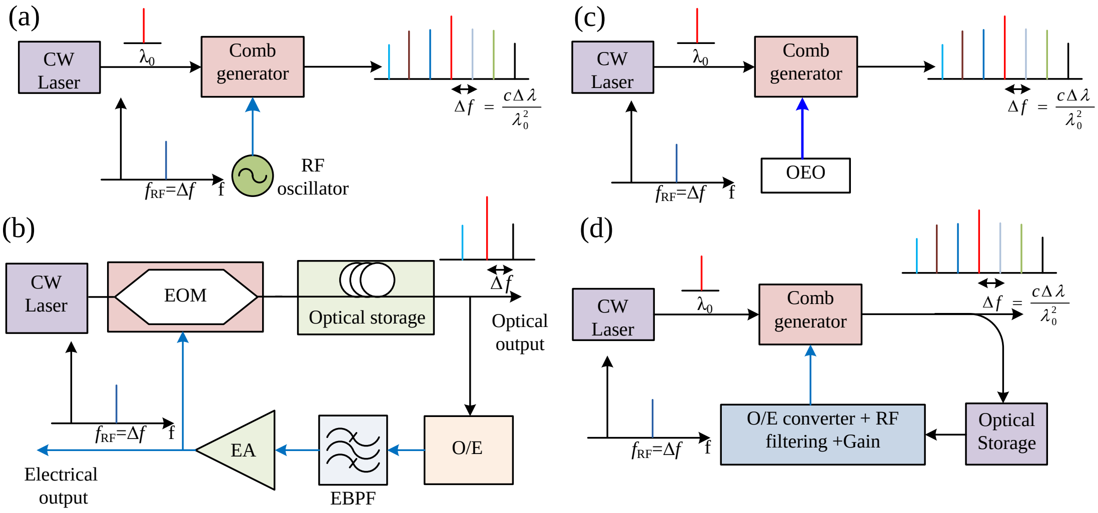

Figure 1 (a) Conventional optical frequency comb generator (OFCG) (b) optoelectronic oscillator (OEO) (c) OEO driven OFCG (d) self-oscillating OFCG. The optical paths are represented by black lines while the electrical paths are represented by blue lines.

2. Mm-wave and THz generation

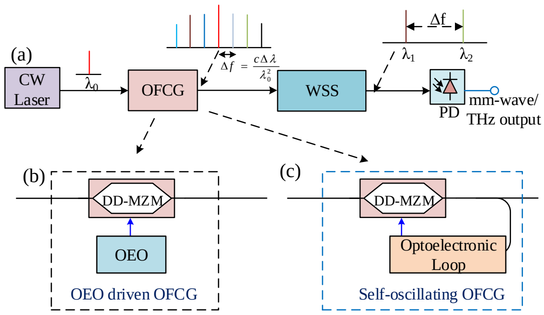

Figure 2. (a) Conceptual diagram of optical frequency comb with optical heterodyning based mm-wave generation. The OFCG block can be realized as an (b) OEO-driven or (c) self-oscillating architecture.

Fig. 2(a) shows the arrangement for generating mm-wave and THz signals with the combination of an OFCG and the optical heterodyne technique. Two optical tones with the desired frequency spacing are selected by a wavelength selective switch (WSS) and then beat in a high speed photo-detector (PD) to generate the electrical signal at the required frequency. Specifically, if $\Delta\lambda$ is the wavelength spacing of the tones then the corresponding frequency Δf that is generated at the PD is given by:

$$\Delta f = \frac{c\Delta\lambda}{\lambda_1\lambda_2}$$

where λ_1 and λ_2 are the wavelengths of the two selected tones. As stated earlier, we have generated an OFC in two scenarios; when the OEO directly drives the OFCG as shown in Fig. 2(b) and a self-oscillating architecture as illustrated in Fig. 2(c). We used a dual-drive Mach-Zehnder modulator as a comb generator where RF signals of different amplitudes and phases are applied to the two RF ports of the DD-MZM [4].

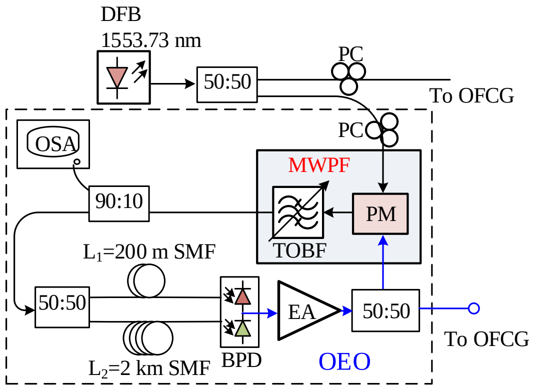

Figure 3. Experimental set-up of OEO-driven OFCG.

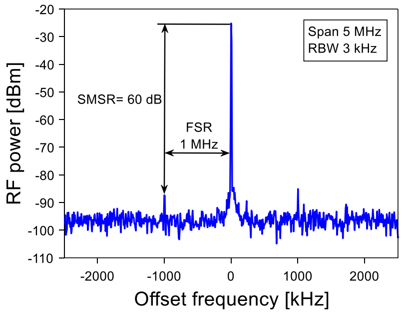

Figure 4. Electrical spectrum of the generated RF signal from an OEO at 17.33 GHz with span of 5 MHz and RBW of 3 kHz.

OEO-driven OFCG:

The OEO block of Fig.2(b) was realized using the arrangement in Fig.3. Light from a DFB laser is routed via a 50:50 coupler to an OEO loop and OFCG. The dual-loop OEO is based on a microwave photonic filter (MWPF). As illustrated in Fig.3, the combination of the phase modulator (PM) and the tunable optical band pass filter (TOBF) functions as microwave photonic filter (MWPF) [5] where the center frequency of the MWPF and hence the oscillation frequency is determined by bandwidth of the TOBF. Amplifiers both in optical and electrical domain are used in the OEO loop to maintain the oscillation condition. By tuning the bandwidth of TOBF we were able to generate the 17.33 GHz oscillation as shown in Fig. 4. The electrical output of the OEO was then connected to the electrical port of a DD-MZM to generate an optical comb. Optical frequency combs are shown in Fig. 5(a) and

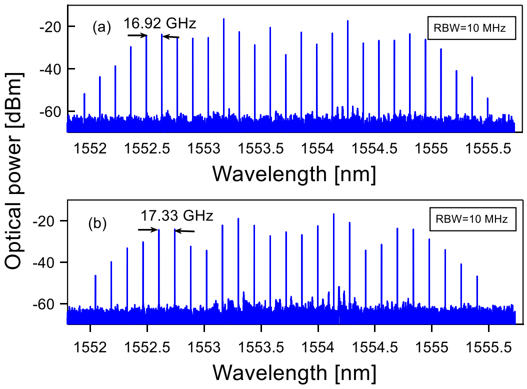

Figure 5. Optical spectra of the generated optical frequency combs with a frequency spacing of (a) 16.92 GHz and (b) 17.33 GHz at the center wavelength of 1553.73 nm

5(b) for the oscillation frequency of 16.92 GHz and 17.33 GHz respectively. We selected two comb lines (from spectrum 5(b)) with a WSS that are spaced 242.6 GHz apart and then beat then in a uni-travelling carrier photo-diode (UTC-PD). The generated electrical signal was then passed through a down-conversion process. The electrical spectrum of the generated 242.6 GHz signal after down-conversion is shown in Fig. 6.

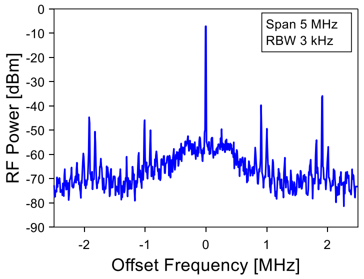

Fig.6. Electrical spectrum of the generated 242.6 GHz signal after down-conversion.

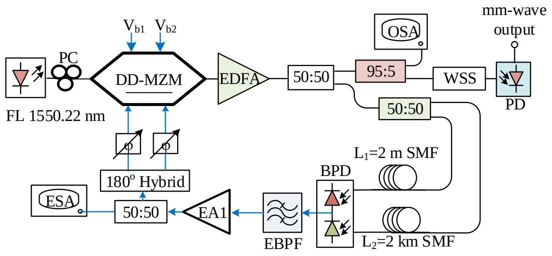

Figure 7. Experimental set-up of self-oscillating OFCG.

Self-oscillating OFCG:

The experimental set-up of a self-oscillating optical frequency comb is shown in Fig.7. An optical signal from a fibre laser was passed through a DD-MZM which functions both as an electro-optic converter in the OEO loop and a comb generator. We used the dual-loop balanced detection in which a dual-loop is used for side-mode suppression [6] and balanced detection is used to suppress common mode noise [7]. An electrical band pass filter with a center frequency of 12 GHz and bandwidth of 300 MHz is used to define the oscillation frequency. Electrical and optical amplifiers are used in the loop to meet the necessary gain condition for oscillation. The optical spectrum of the self-oscillating OFCG is shown in Fig.8 with a frequency spacing of 11.84 GHz; 23 comb lines were generated with 12 dB deviation. The electrical spectrum of the 11.84 GHz signal is shown in Fig.9(a). To generate a mm-wave signal we selected two comb lines (red and blue lines of Fig.8) and at the output of the photo-diode an electrical signal of 94.8 GHz was generated, the electrical spectrum of which is shown in Fig.9(b).

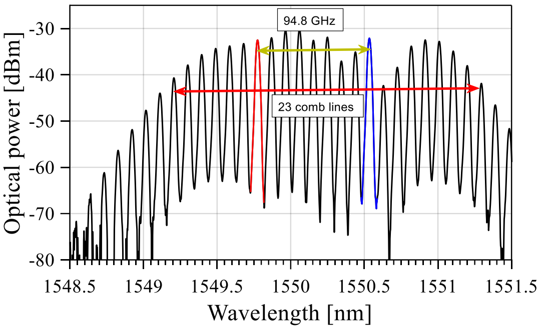

Figure 8. Optical spectrum of the self-oscillating OFCG with 23 comb lines spaced at 11.84 GHz. The red and blue lines are the selected tones for mm-wave generation and radio over fibre link.

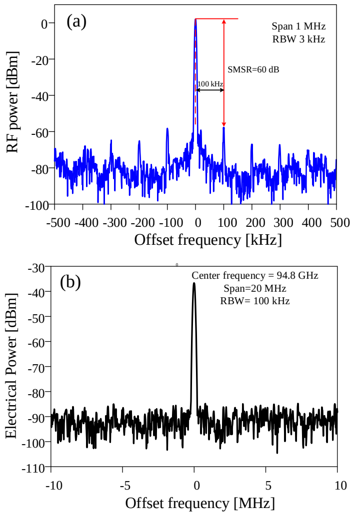

Figure 9. Electrical spectrum of the generated RF signal (a) from self-oscillating OFCG at 11.84 GHz (b) 94.8 GHz

3. Radio over fibre link

We implemented a RoF link based on the self-oscillating OFCG. The conceptual diagram is shown in Fig. 10. We selected two comb lines generated from the SOFCG with WSS at 94.8 GHz separation (red and blue lines of Fig.8) and directed them to two different ports of the WSS; one of the tones was data modulated while the other tone was transmitted for heterodyning. A standard LTE advanced signal centered at 1 GHz and a bandwidth of 20 MHz and 64 QAM modulation format was used as a

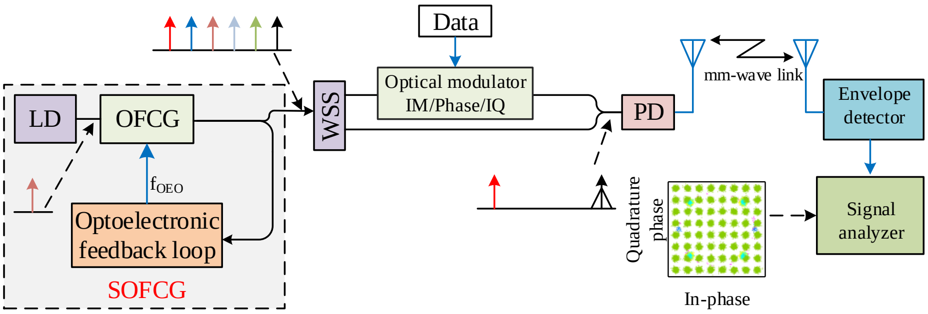

Figure 10. Block diagram of a SOFCG based radio over fibre link. LD - Laser diode, WSS -Wavelength selective switch, IM - Intensity modulation, PD - Photodetector

modulating signal generated from an Agilent PSG vector signal generator (E8267D). The two tones were then combined, amplified and detected in a high-speed photo-detector. The generated mm-wave signal at 94.8 GHz was transmitted over a 1.3 m wireless path through a set of horn antennas with a gain of 23 dBi. The received mm-wave signal was then amplified by a low noise amplifier, down-converted by an envelope detector and analyzed by a vector signal analyzer. We used a variable optical attenuator prior to the photo-detector to adjust the input optical power and hence the photo-current. We measured the error vector magnitude (EVM) at different photo currents as depicted in Fig.11. The measured EVM is within the limit of the ITU recommendation (8% for 64 QAM) for the photo-current above 0.6 mA.

4. Conclusions

We have considered two scenarios of an OFCG; an OEO-driven and a self-oscillating architecture. In the self-oscillating OFCG, a single DD-MZM functions as both an E/O converter and a comb generator, whereas in the separately OEO-driven system two separate modulators are required (one for the OEO loop and another for the comb generator).

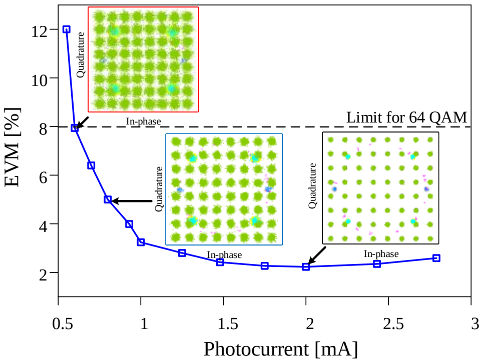

Figure 11. EVM vs photocurrent of the self-oscillating OFCG based RoF system. The insets are the constellation diagram of (64 QAM OFDM signal, 1.3 m wireless transmission distance).

5. References

[1] G. K. M. Hasanuzzaman, A. Kanno, P. T. Dat, and S. Iezekiel, “Self-oscillating optical frequency comb: Application to low phase noise millimeter wave generation and radio-over-fiber link,” *J. Light. Technol.*, vol. 36, no. 19, pp. 4535–4542, 2018.

[2] G. K. M. Hasanuzzaman, H. Shams, C. C. Renaud, J. C. Mitchell, and S. Iezekiel, “Photonic THz Generation using Optoelectronic Oscillator-driven Optical Frequency Comb Generator,” in *2018 International Topical Meeting on Microwave Photonics (MWP)*, 2018, pp.1–4.

[3] X. S. Yao and L. Maleki, “Optoelectronic microwave oscillator,” *J. Opt. Soc. Am. B*, vol. 13, no. 8, pp. 1725–1734, Aug. 1996.

[4] T. Sakamoto, T. Kawanishi, and M. Izutsu, “Asymptotic formalism for ultraflat optical frequency comb generation using a Mach-Zehnder modulator.,” *Opt. Lett.*, vol. 32, no. 11, pp. 1515–1517, 2007.

[5] T. Chen, X. Yi, L. Li, and R. Minasian, “Single passband microwave photonic filter with wideband tunability and adjustable bandwidth.,” *Opt. Lett.*, vol. 37, no. 22, pp. 4699–701, 2012.

[6] X. S. Yao and L. Maleki, “Multiloop optoelectronic oscillator,” *IEEE J. Quantum Electron.*, vol. 36, no. 1, pp. 79–84, 2000.

[7] F. Fan, J. Hu, W. Zhu, Y. Gu, X. Han, and M. Zhao, “Dual-loop optoelectronic oscillator based on a compact balanced detection scheme,” *Opt. Eng.*, vol. 56, no. 2, p. 026107, Feb. 2017.

Microwave Antennas on Electro-Optic Modulators for Wireless Electromagnetic Measurement

Yusuf Nur WIJAYANTO
Research Group on RF, Microwave, Acoustic, and Photonic
Research Center for Electronics and Telecommunication
Indonesian Institute of Sciences (LIPI)
Jl. Sangkuriang Cisitu, Bandung 40135 INDONESIA
yusuf.nur.wijayanto@lipi.go.id

Abstract –Recently, electromagnetic (EM) wave pollution in air are important issue for human welfare and health. Wireless EM wave in air should be monitored and regulated by government by following international standards. The key device for sensing the wireless EM wave is an antenna. In here, wireless microwave antennas on electro-optic (EO) modulators are presented and discussed. Several type antenna structures fabricated in EO modulators such as patch, slot, yagi, and metamaterial are reported. This device has advantages of low microwave distortion and no microwave induction also directly converted to lightwave signal in the EM measurement system.

Keywords – EM measurement; microwave antenna; EO modulator;

1. Introduction

Electromagnetic measurement is required for measuring characteristics of the radiated electromagnetic (EM) in our world. The EM radiation in air should be monitored to minimize EM pollution or unwanted radiated EM [1]. The EM can be radiated by following world standardization which are regulated by the government. In the EM measurement need an EM sensor for identifying EM characteristics with precise sensing and low induction.

Recently, the EM sensor consists of an antenna or probe where can detect the generated or radiated EM from the device under test (DUT) [2,3]. The EM measurement is developed and applied in technology with microwave bands to measure current available electronic equipment in the market. In the near future, high-quality, high-speed, and high-resolution are the user demands in communication and imaging applications. Bandwidth enhancement can meet the user demands by using high-frequency operation. In order to anticipate it, high-frequency EM measurement should be prepared. The high-frequency EM sensors are also required.

In this paper, wireless EM sensors using microwave antennas on electro-optical (EO) modulators are presented for wireless EM measurement. Several types of microwave antennas on EO modulators are discussed such as patch, slot, quasi yagi, and metamaterial types. The design, fabrication, and characterization of the EM sensing devices are reported. Typical applications in wireless EM measurement are also briefly described.

2. Patch Antennas Coupled with EO Modulators

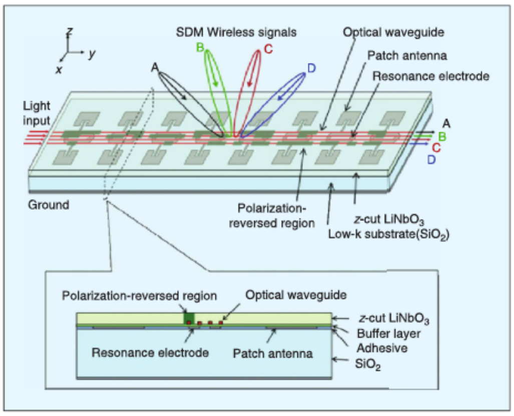

Fig. 1 Typical structure of patch Antennas with EO modulators.

Several devices using patch antennas coupled with EO modulators were reported [4,5]. Figure 1 shows the patch antennas coupled with EO modulators. The device is fabricated on a *z*-cut $LiNbO_3$ optical crystal. It has advantages to identify wireless EM irradiation angle by manipulating interaction between microwave and lightwave signals along the modulation electrodes with polarization reversal techniques. The typical experiment results of the fabricated devices is shown in Fig. 2 where several wireless EM irradiation angle pattern can be observed. Therefore, the devices can be used for wireless EM measurement.

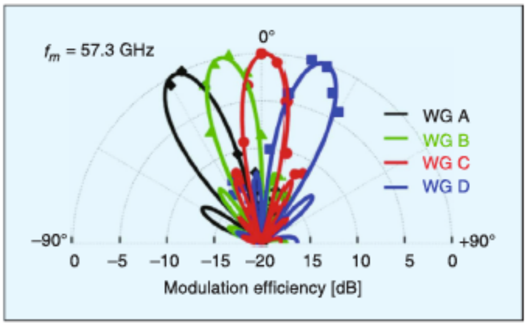

Fig. 2 Experimental results for wireless EM characterization.

3. Slot-antennas on EO Modulators

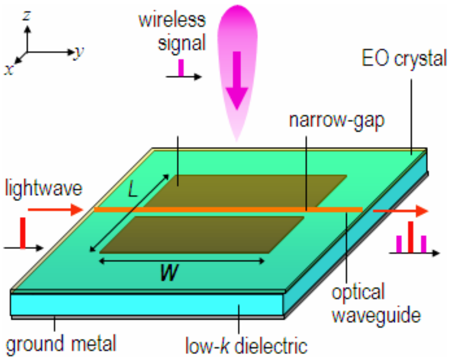

Fig. 3 Typical structure of slot antennas on EO modulators.

We have reported also the devices using slot-antennas on EO modulators [6,7]. Fig. 3 shows the slot antennas on EO modulator. His device can be used for detecting wireless microwave and converting it directly to lightwave signal. Very low microwave loss can be achieved using the device. The typical measurement result of the optical modulation by irradiating wireless microwave is shown in Fig. 4. The device can be used for detecting wireless EM through optical modulation.

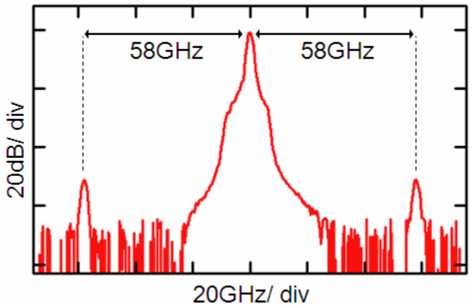

Fig. 4 The measured wireless EM on lighwave signal

4. Quasi Yagi Antennas with EO Modulators

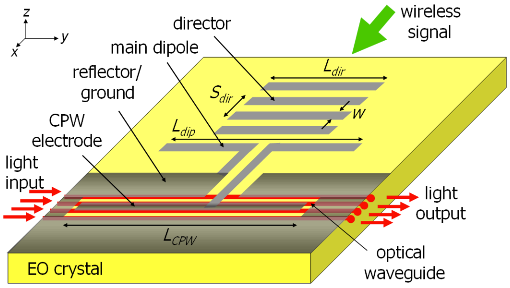

Fig. 5 The structure of quasi yagi antennas with EO modulators.

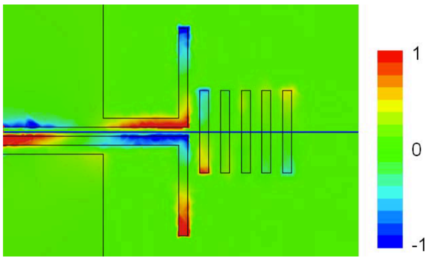

Fig. 6 The calculated electric field distribution on the EO substrate.

We designed the wireless EM sensor using quasi yagi antennas with EO modulators [8]. It consist of planar yagi antennas coupled with standing-wave EO modulators as shown in Fig, 5. This device has high sensitive EO sensors due to high-gain characteristics of the yagi antenna.

5. Metamaterial Antennas on EO Modulators

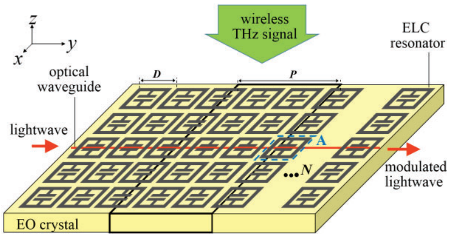

Fig. 7 The structure of metamaterial antenna on EO modulators.

Figure 7 shows the device using metamaterial antennas on EO modulators [9]. The device consists of a straight optical waveguide and ELC resonators fabricated on an EO crystal. It can be used for receiving wireless high-frequency microwave and converting it to loghtwave. The device has easy design for high-frequency operation especially. The typical

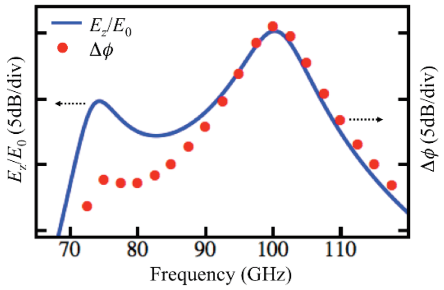

Fig. 8 The calculated modulation index of the wireless EM sensor.

6. Summary

We have reported wireless EM sensors using microwave antennas on EO modulators for wireless EM measurement. Several type antennas were used for wireless EM detector and converted it to lightwave using EO modulation. By using this technique, low microwave distortion and no microwave induction can be achieved for wireless EM measurement system.

Acknowledgments

The author would like thanks to Prof Yasuyuki Okamura (Osaka Univ.) and Prof. Hiroshi Murata (Mie Univ.) for their supervising and guiding. Thanks to Prof. Tetsuya Kawanishi (Waseda Univ.) and Dr. Atsushi Kanno (NICT) for their great support and discussion. Also thanks to Dr. Purwoko Adhi, Pamungkas Daud, Dadin Mahmudin, and Ashif Aminullah Fathnan from Indonesian Institute of Sciences (LIPI) for their help in calculation and analysis.

References

[1] W.O. Henry, "Electromagnetic compatibility engineering," John Wiley & Sons, Inc, 2009.

[2] M. Ameya, S. Kurokawa, and M. Hirose, "Millimeter-wave antenna pattern measurement using high extinction ratio Mach-Zehnder modulator," 6th European Conference on Antennas and Propagation, pp 2574-2577, 2012.

[3] S. Shinada, T. Kawanishi, and M Izutsu, "A resonant type LiNbO3 optical modulator array with micro-strip antennas," IEICE Trans. Electron., vol. E90-C, no. 5, pp. 1090–1095, May 2007.

[4] H. Murata, N. Kohmu, Y. N. Wijayanto, Y. Okamura, "Integration of Patch Antenna on Optical Modulators," IEEE Photonics Society News, vol. 28, no. 2, April 2014.

[5] F. T. Sheehy, W. B. Bridges, and J. H. Schaffner, "60 GHz and 94 GHz antenna-coupled LiNbO3 electrooptic modulators," IEEE Photon. Technol.Lett., vol. 5, no. 3, pp. 307–310, Mar. 1993.

[6] Y. N. Wijayanto, A. Kanno, H. Murata, T. Kawanishi, N. Yamamoto, and Y. Okamura, "Array of Patch-Antennas with Meandering-Gaps on Optical Modulator for Wireless Millimeter-Wave Beam-Steering ," International Journal of Microwave and Wireless Technologies, Volume 8, Special Issue 4-5, pp 759-765, June 2016

[7] Y. N. Wijayanto, H. Murata, and Y. Okamura, "Electro-Optic Millimeter-Wave-Lightwave Signal Converters Suspended to Gap-Embedded Patch Antennas on Low-k Dielectric Materials," IEEE Journal of Selected Topics in Quantum Electronics., vol.19, no.6, November/ December 2013

[8] Y. N. Wijayanto, H. Murata, and Y. Okamura, "Electro-Optic Wireless Millimeter-Wave-Lightwave Signal Converters Using Planar Yagi-Uda Array Antennas Coupled to Resonant Electrodes," in 17-th Opto-Electronic Communications Conference, 5E1-2, Busan – Korea, 2-6 July 2012

[9] Y.N. Wijayanto, A. Kanno, A.A. Fathnan, P. Daud, T. Kawanishi, D. Mahmudin, and N. Yamamoto "Metamaterial Antenna Integrated to LiNbO3 Optical Modulator for Millimeter-Wave-Photonic Links," International Symposium Antenna and Propagation (ISAP) 2015, Tasmania, Nopember 2015.

Photodiode calibration up to 100 GHz based on electro-optic sampling for national waveform standard

Dong-Joon Lee, Chihyun Cho and Young-Pyo Hong
Division of Physical Metrology, Korea Research Institute of Standards and Science
Yuseong-gu, Daejeon 34113, Republic of Korea

*Corresponding author: dongjoonlee@kriss.re.kr

Abstract –We present a pulse waveform metrology system based on electro-optic sampling at the Korea National Institute of Standards and Science (KRISS). A fast pulse measurement system using a femtosecond laser and a photodiode up to 100 GHz bandwidth has been implemented. We adopted this photodiode and system to generate and measure standard pulse waveform. The photodiode was calibrated in full 100 GHz bandwidth for utilization in transfer standard pulse generation for the Korean national standard.

Keywords – electro-optic; pulse waveform; on-wafer probing; impedance calibration

1. Introduction

Conventional fast pulse waveform metrology based on electrical sampling oscilloscopes has been considered a challenging task. This is mainly because the calibration method is not well-established beyond 50 GHz. One excellent breakthrough is the technique of electro-optic sampling (EOS). EOS employs a femtosecond pulsed laser source that can realize even sub-ps ultrafast transient sampling. Thus, the EOS technique has evolved into a mature solution for Terahertz science.

National Metrology Institutes (NMIs) have adopted this technique to enhance their calibration bandwidth of waveform metrology up to 100 GHz (or beyond) for employment as primary standards for high-speed waveforms. The National Institute of Standards and Technology (NIST) of the US was the first to use an EOS system with a 100 GHz high speed photodiode (PD) [1,2]. Other major NMIs – PTB of Germany, NPL of the UK, and NIM of China – have also built their own EOS systems associated with high speed photodiodes for calibration service and measurement capability enhancement [3-5].

Fig.1 explains the traceability chain for the waveform transfer standard. The calibrated PD associated with the EOS system serves as a primary pulse standard for each NMI. Such primary standards are utilized to make secondary standards or to calibrate customers' instruments.

NMIs compare their EOS systems with others to validate their own standards. NIST, PTB, and NPL have compared their results and, recently, NIM and KRISS joined the comparison group to corroborate their systems [5].

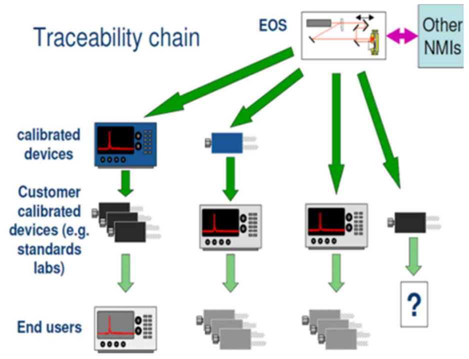

Figure 1. Traceability chance for pulse standard in NMIs (from NPL website)

2. KRISS EOS system

We at KRISS also launched time domain EOS research in 2013. Our EOS for 100 GHz pulse waveform metrology is illustrated in Fig.2. This is implemented with a pump-probe style interferometric scheme. As a national standard system, uncertainty and system stability are major concerns for metrology grade systems in NMIs. We used dual variable attenuators at the pump and probe paths. Optical instability, which degrades measurement reliability, is monitored and stabilized during measurement by programmable attenuators.

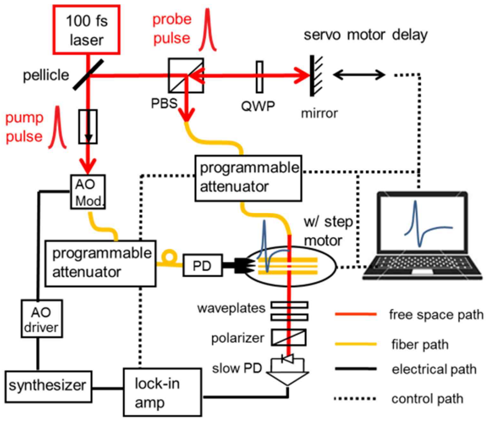

Figure 2. KRISS EOS system for 100 GHz pulse waveform metrology.

Pump pulse is used to excite a fast photodiode with 100 GHz bandwidth. The fast electrical pulse from the photodiode is delivered from its intrinsic 1 mm coaxial port to a coplanar waveguide on an x-cut $LiTaO_3$ wafer through a GSG style on-wafer probe.

To serve as a primary transfer standard, a waveform with perfect 50 ohm mating at the PD output port needs to be characterized. Although there is no way to measure this directly, the pulse travelling along the line on the EO wafer can be precisely measured instead. The measured pulses become inherently non-invasive because the waveguide itself on the EO wafer works as a sensor. We present such pulses on the wafer and techniques to obtain precise response at the PD port by compensating for errors in the measurement system.

3. Results and Discussion

The 100 GHz pulses are generated by our fast PD (u2t: XPDV4120R), which is excited by ~100 fs laser pump pulses. The pulses from the diode are launched onto a coplanar waveguide made with EO substrate, as shown in the inset of Fig.3. The probe pulses in the EOS system sample the 100 GHz pulses in a reconstructed pulse shape with a 10 μm translation step. The pulse needs to be measured at both gaps in the coplanar waveguide (CPW). The results are averaged to cancel the undesired mode effect in the CPW. The measured and mode-cancelled pulses are presented in Fig.3.

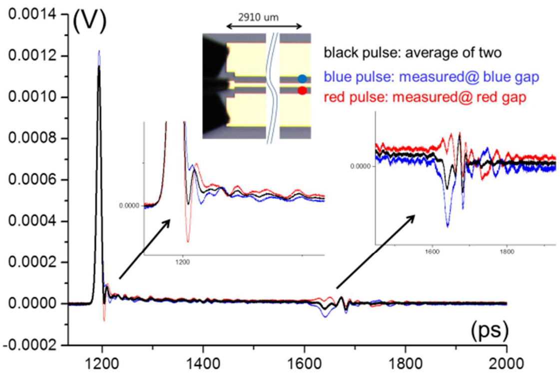

Figure 3. Measured pulse from the fast photodiode on EO wafer with KRISS EOS system.

One of main factors that affects pulse measurement is mismatch at the on-wafer probe tip and the pads of the CPW. The pad quality degrades for every probe contact, which ruins repeatability. The insets in Fig.4 show that mismatch causes secondary pulses, raising a concern about repeatability.

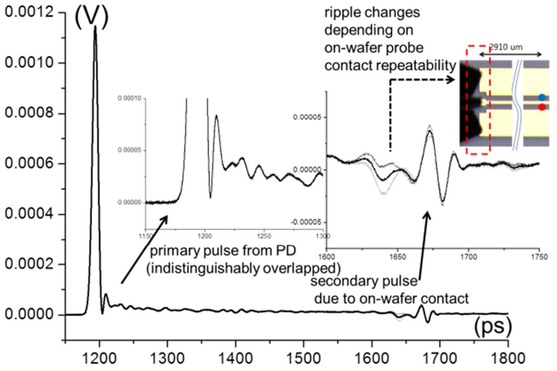

Figure 4. Measured pulse from fast photodiode with KRISS EOS system.

The microwave transmission characteristics from the PD port to the measurement spot must be thoroughly measured with uncertainty analysis. We designed and fabricated TRL calibration kits on the same EO wafer. Fig.5 shows our on-wafer probe station to measure S-parameters up to the W-band. Therefore, spectral components with phase information can be de-embedded up to the PD port.

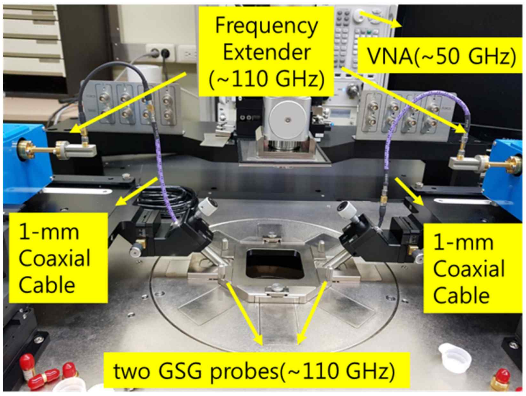

Figure 5. KRISS on-wafer probe station for TRL calibration.

In addition to microwave impedance error correction, the EO system itself must be calibrated. This is mainly because the ~100 fs Gaussian laser pulses broaden as they propagate through dispersive optical fibers. The broadened pulse widths at pump and probe sides were measured at ~3400 fs and ~6450 fs, respectively. Pump broadening slows the optical excitation of the PD. For a similar reason, probe broadening degrades the sampling measurement speed. Fig.6 shows the spectral response due to pump and probe broadening with 10 % uncertainty. This optical response must be systematically de-convoluted to obtain an impulse response in the EOS measurement associated with the femtosecond laser.

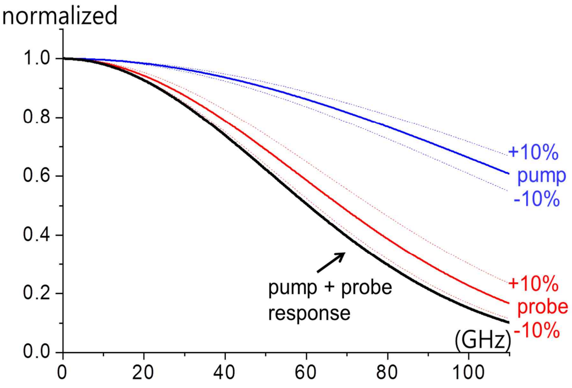

Figure 6. EO system response for pump/probe pulse broadening.

Considering both microwave and optical system error-corrections (i.e., de-embedding and de-convolution), the spectral response from the measured pulse is corrected as shown in Fig.7.

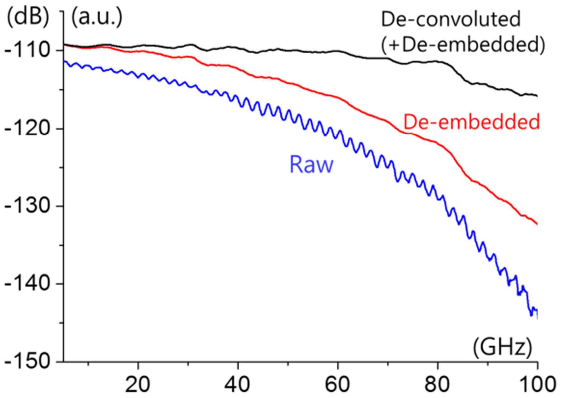

Figure 7. Spectral response of PD with 100 GHz bandwidth.

The genuine spectral response of the PD with expanded uncertainty (k=2) is presented in Fig.8. The magnitude is normalized to the mean in the frequency range from 5 GHz to 100 GHz. As a transfer standard, the PD should present its uncertainty. For microwave uncertainty, noise floor/trace-noise/linearity in a VNA device, on-wafer cable stability, on-wafer crosstalk, and definitions of calibration standards are considered. For optical uncertainty, probe beam position, pump/probe beam stability, type A uncertainty, multiple reflection due to $LiTaO_3$ wafer surfaces, and time delay jitter error due to probe translation stage are considered. Finally, the uncertainty due to pump-probe de-convolution is included.

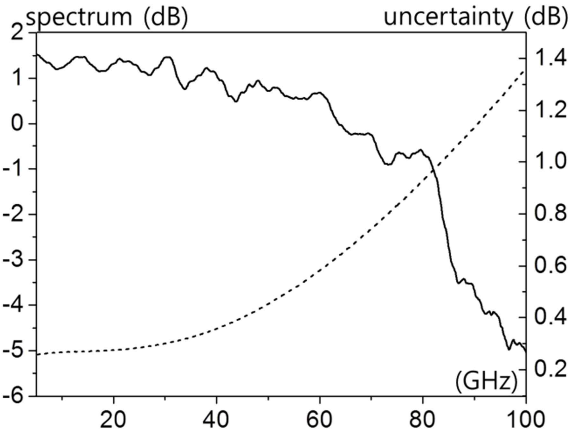

Figure 8. Normalized spectral response of PD with 100 GHz bandwidth with expanded uncertainty (k=2).

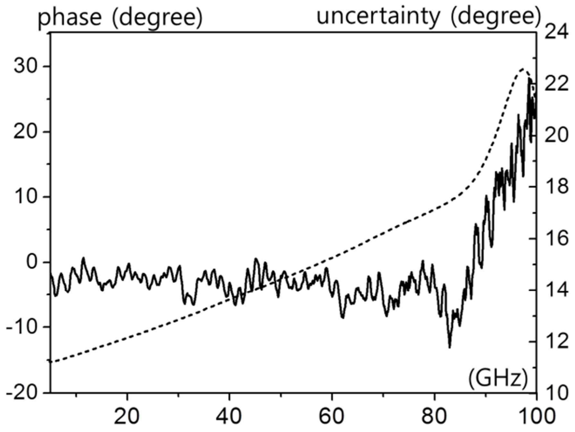

Figure 9. Frequency-domain phase of PD with 100 GHz bandwidth with expanded uncertainty (k=2).

To validate our results, this PD (u2t: XPDV4120R, SN: 10125001) has since 2018 been measured among five different NMIs including KRISS. The comparison is completed as of August 2019 and the inter-comparison results are to be released during the presentation.

4. Conclusions

We briefly introduced the EOS system for a 100 GHz pulse standard at KRISS. A photodiode calibrated using this system serves as a time and frequency-domain transfer standard and allows for subsequent calibration of high-speed oscilloscopes and high-speed modulated signals.

References

[1] Williams D, Hale P, Clement T, Morgan J, Calibrated 200-GHz waveform measurement. 2005 IEEE Trans. Microw. Theory Tech. 2005; 53(4):1384–1389.

[2] Clement T, Hale P, Williams D,, Wang C, Dienstfrey A, Keenan D, Calibration of sampling oscilloscopes with high-speed photodiodes. Trans. Microw. Theory Tech. 2006; 54(8):3173–3180.

[3] Seitz S, Bieler M, Spitzer M, Pierz K, Hein G and Siegner U, Optoelectronic measurement of the transfer function and time response of a 70 GHz sampling oscilloscope. Meas. Sci. Technol. 2005; 16(10):L7–L9.

[4] Feng Z, Zhao K, Yang Z, Miao J, Chen H, 100 GHz pulse waveform measurement based on electro-optic sampling. Laser Phys. 20018; 28:055301–5.

[5] Hale P, Williams D, Dienstfrey A, Wang J, Jargon J, Humphreys D, Harper H, Füser H, Bieler M, Traceability of high-speed electrical waveforms at NIST, NPL, and PTB," 2012 Conference on Precision electromagnetic Measurements. 2012: 522–523.

Performance Evaluation of Electric-Field Sensor for Power Density Measurement by Back-projection Method

Michitaka AMEYA
NMIJ, National Institute of Advanced Industrial Science and Technology, Tsukuba, Ibaraki, 305-8563 Japan
*Corresponding author: m.ameya@aist.go.jp

Abstract – In recent years, electric field sensors have attracted attention again for purposes such as 5G power density measurement. When using an electric field sensor, not only calibration of the sensitivity of the sensor but also evaluation of the receiving pattern is important. In this paper, we focus on the application to antenna measurement and power density measurement in near-field, and report on the effect of the receiving pattern of the electric field sensor on the measurement results.

Keywords – Electric-field sensor calibration, Pattern evaluation, Near-field measurement;

1. Introduction

In recent years, electric field sensors have attracted attention again for purposes such as 5G power density measurement. When using an electric field sensor, not only calibration of the sensitivity of the sensor but also evaluation of the receiving pattern is important. In this paper, we focus on the application to antenna measurement and power density measurement in near-field, and report on the effect of the receiving pattern of the electric field sensor on the measurement results.

2. Application of electric-field sensor

The applications of electric field sensors have been the main needs so far for evaluating the uniformity of electric fields in radiation immunity tests [1] and measuring radiation patterns of antennas in near-field [2]. It has been decided that it will be used to measure the power density of mobile terminals for human exposure, and the international standard is now under discussion [3]. As the measurand of the electric field sensor, the absolute electric field strength is a typical calibration target, but isotropy, cross polarization discrimination level, and receiving pattern are also important. This time, we focused on the receiving pattern and investigated the effect of the difference on the estimation result of power density.

3. Antenna Element Shape v.s. Receiving pattern of electric-field sensor

The radiation pattern of the antenna for electric field sensor was calculated by MoM. The structures of electric field sensors are shown in Fig. 1 (a), (b), and (c). We calculated WR28 open ended waveguide (abbreviated as OEWG), 0.2λ dipole, 1.0λ dipole, and 0.1λ monopole antenna on 1.0 λ chassis at 30 GHz.

Fig.2 shows the frequency characteristics of the antenna gain of each antenna, and Fig. 3 shows the radiation patterns for each antenna on the E and H planes. As can be seen from the figure, the directivity gain is highest in the OEWG, which is 5.5 dBi to 7.7 dBi, which is the most sensitive result than other three sensors.

In the case of the dipole type sensor, a uniform pattern is obtained in the azimuth direction. On the other hand, in the case of OEWG, the beam is focused on both the horizontal plane and the vertical plane, but the beam is relatively wide. It can be seen that the maximum radiation direction of the monopole antenna with a chassis is inclined in the direction of $\theta = 75$ degrees.

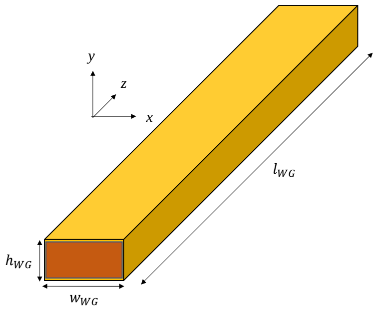

(a) OEWG

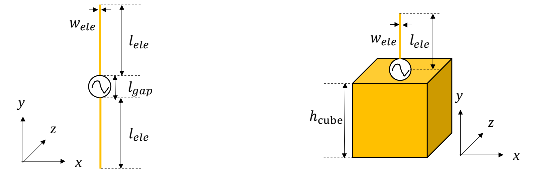

(b) 0.2 λ or 1.0 λ dipole (c) 0.1 λ monopole with chassis

Fig.1 Element structure of Electric-field sensors

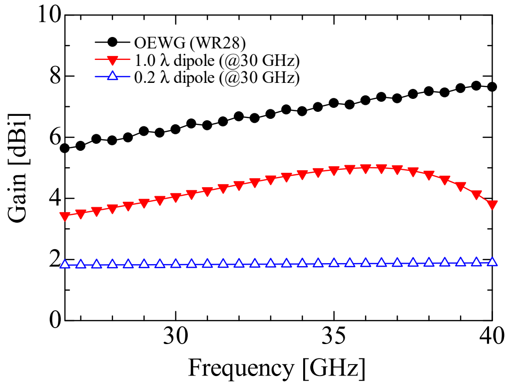

Fig.2 Frequency characteristics of Antenna directivity

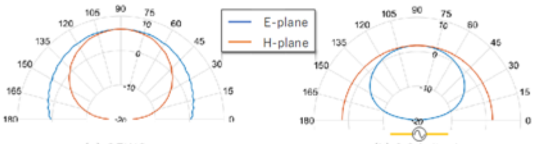

(a) OEWG (b) 0.2 λ dipole

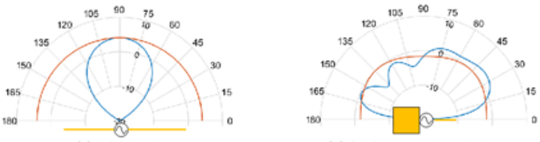

(c) 1.0 λ dipole (d) 0.1 λ monopole with chassis

Fig.3 Receiving Pattern of Electric-field sensors.

4. Effect of Receiving Patten on Power density measurement by Back-projection method

In power density measurement for human exposure, it has been studied to estimate the power density at a position of 5 mm to 20 mm from the antenna. However, it is difficult to directly measure the electric field near the antenna with a sensor. The electric field at a distance of 5λ to 10λ is measured, and the power density at 5 mm to 20 mm is estimated by the back-projection method [2].

In the back-projection method, the observation plane can be changed to an arbitrary z-position by first converting the electric field strength into a plane wave spectrum and then changing only the phase term in the z direction.

The 16-element patch antenna shown in Fig. 4 was simulated by MoM and the electric field distribution of z = 50 mm and z = 5 mm were calculated. The calculation results are shown in Fig.5.

Fig. 6 shows the electric field distribution at z = 5 mm, which is obtained by simulating electric field measurement results using various sensors and reproduced by the back-projection method. The difference from the calculation result by MoM is shown in Fig. 7.

Table 2 shows the average and maximum differences within the antenna area (within ± 13 mm or less). From Table 2, the average difference was 6.7% for 0.2λ dipole, 8.5% for OEWG, and 9.7% for 1.0λ dipole. In the case of a 0.1λ monopole with chassis, the position of the distribution shifts in the -y direction, and it can be seen that the correct result is not obtained.

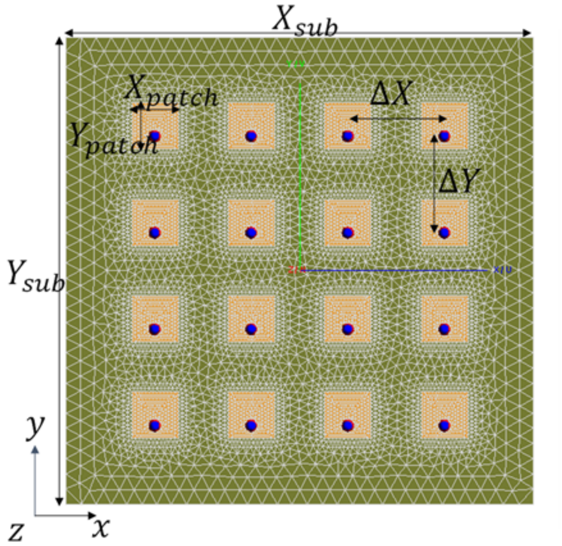

Fig.4 Structure of 4x4 Patch Antenna

Table 1 Design Parameter of 4x4 Patch Antenna

	Value	Explanation
f	30 GHz	Frequency (λ =10 mm)
X_{sub}	26 mm	Width of substrate
Y_{sub}	26 mm	Height of substrate
h_{sub}	0.4 mm	Thickness of substrate
X_{patch}	2.57 mm	Width of patch
Y_{patch}	2.57 mm	Height of patch
ΔX	5.3715 mm	Element spacing in x-direction
ΔY	5.3715 mm	Element spacing in y-direction
ε_r	3.5	Dielectric constant of substrate
N_x	4	Number of element in x-direction
N_y	4	Number of element in y-direction
Δx_{meas}	0.5 mm (= 0.05λ)	Sampling interval in x-direction
Δy_{meas}	0.5 mm(= 0.05λ)	Sampling interval in y-direction
x_{meas}	-100 mm to 100 mm	Measurement range in x-direction
y_{meas}	- 100 mm to 100 mm	Measurement range in y-direction
z_{meas}	50 mm	Measurement height

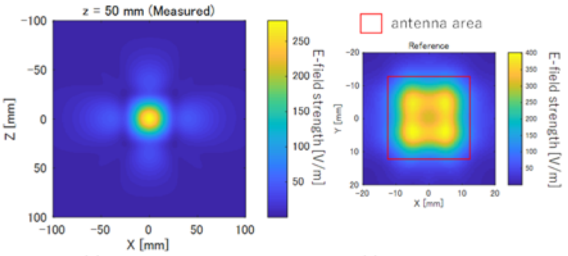

(a) E_y at z = 50 mm (b) E_y at z = 5 mm

Fig.5 Simulation results of Electric field at z = 50 mm and z = 5 mm by MoM

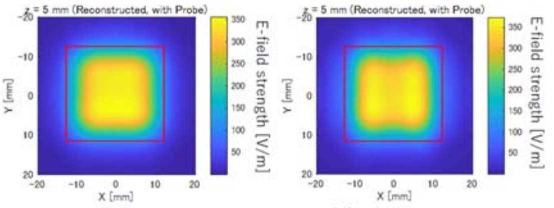

(a) OEWG (b) 0.2 λ dipole

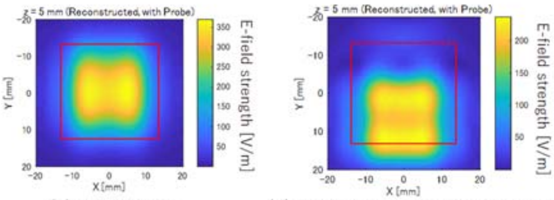

(c) 1.0 λ dipole (d) 0.1 λ monopole with chassis

Fig.6 Estimated Electric-field by electric-field sensors at z = 5 mm.

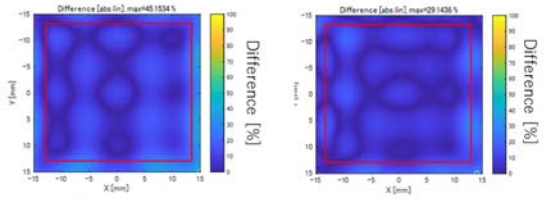

(a) OEWG (b) 0.2 λ dipole

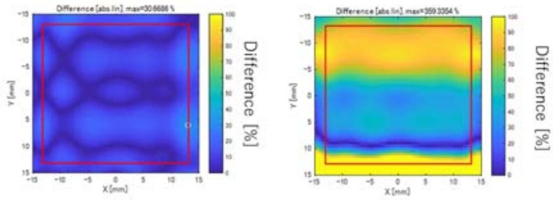

(c) 1.0 λ dipole (d) 0.1 λ monopole with chassis

Fig.7 Difference between estimated electric-field distribution by back-projection method and directly simulated electric-field distribution by MoM

Table 2 Average difference and Maximum difference.

	Avg. Difference [%]	Max. Difference [%]
OEWG (WR28)	8.5	31.5
0.2 λ dipole	6.7	26.3
1.0 λ dipole	9.6	30.7
0.1 λ monopole with chassis	62.4	232.4

5. Conclusions

In this paper, we investigated the effect of the receiving pattern of the electric field sensor on the measurement result of the power density estimation. It was found that

0.2λ dipole has the highest accuracy when probe correction is not performed. In the monopole type sensor, since the maximum receiving angle does not face the front, it became clear that there is a difference in the position of the electric field distribution after back-projection. From these results, it has been clarified that when designing an electric field sensor, it is necessary to consider the feeding balance of the element and the symmetry of the receiving pattern.

References

[1] IEC 61000-4-3, “Electromagnetic compatibility (EMC)- Part4-3: Testing and measurement techniques- radiated, radio-frequency, electromagnetic field -immmunity test, 3rd edition, 2006.

[2] Stuart Gregson, John McCormick, Clive Parini, Principles of Planar Near-field Antenna Measurements, IET, 2007.

[3] IEC, P63195 - IEEE/IEC Draft Standard Measurement procedure for the assessment of power density of human exposure to radio frequency fields from wireless devices operating in close proximity to the head and body - Frequency range of 6 GHz to 300 GHz, 2019.

Phase Measurement of Millimeter-Wave 3-tone Signal using Electro-Optic Frequency Conversion with Bandwidth Reduction

Takashi Mori* and Shigenori Mattori
Advanced Technology Development Center, Technical Headquarters, Anritsu Corporation
5-1-1 Onna, Atsugi City, Kanagawa, 243-8555 Japan
*Corresponding author: tmori@ieee.org

Abstract — A phase measurement method for millimeter-wave 3-tone signals using electro-optic frequency conversion is presented for phase calibration of frequency converters. A three-frequency optical local signal instead of a conventional single-frequency local signal was used for down conversion with bandwidth reduction. A 300-GHz band 3-tone signal with 100-MHz spacing was converted to 1.5-Hz I/Q signals with 4-Hz spacing that can be digitized using a low sampling rate of 50 sample/s. The phase measurement results matched the theoretical phase, accounting for 3rd-order nonlinearity, and the standard deviation of the measured phase was less than 1 degree.

Keywords — electro-optic crystal; frequency conversion; millimeter wave; phase calibration; multitone signal

1. Introduction

High-capacity wireless networks are required to handle the huge increase in data traffic from increasing numbers of mobile terminals. High-carrier-frequency signals, such as millimeter wave (mmWave) or THz wave, are effective for increasing data rates [1]. Since wireless networks commonly use multilevel modulation to improve spectral efficiency, accurate measurement of mmWave signals is required in the near future.

mmWave frequency converters in test equipment usually have imperfect frequency characteristics and should be calibrated for precise measurement. Although amplitude characteristics can be calibrated easily using a mmWave calorie meter, phase characteristics are difficult to calibrate due to need for waveform measurement. The electro-optic (EO) sampling method using an EO crystal and a short optical pulse has been proposed for measuring waveforms of high-frequency signals without using electrical mixers [2], [3]. We have proposed a phase calibration method by measuring mmWave 3-tone signals using EO sampling [4]. However, the measurement frequency resolution is limited by the sampling time span. On the other hand, photonics-based frequency conversion has also been proposed using either an EO crystal [5], [6] or photoconductive antenna [7] as a harmonic mixer. Although the frequency-conversion method can measure waveforms with high frequency resolution, the intermediate frequency (IF) signal, which has the same bandwidth as the radio frequency (RF) signal, is affected by the frequency characteristics of electrical circuits downstream from frequency conversion.

This presentation describes a phase measurement method using EO frequency conversion with bandwidth reduction, and discusses phase measurement results of mmWave 3-tone signals [8] for phase calibration.

2. Principle of EO frequency conversion

Figure 1 shows the principle of conventional EO frequency conversion. The measured RF signal is a 3-tone signal with carrier frequency f_{RF} and frequency spacing f_m; the optical local signal consists of two continuous-wave (CW) signals with frequency spacing $f_{\mathrm{LO}} = f_{\mathrm{L2}} - f_{\mathrm{L1}}$. A photodiode (PD) detects polarization changes of the reflected light due to the EO effect, and the PD output is proportional to product of the optical local signal intensity and electric field. Hence, the RF signal frequency f_{RF} is

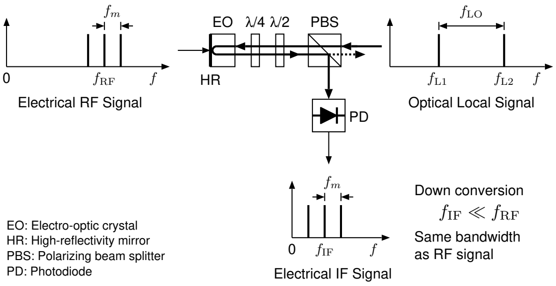

Figure 1. Conventional EO frequency conversion

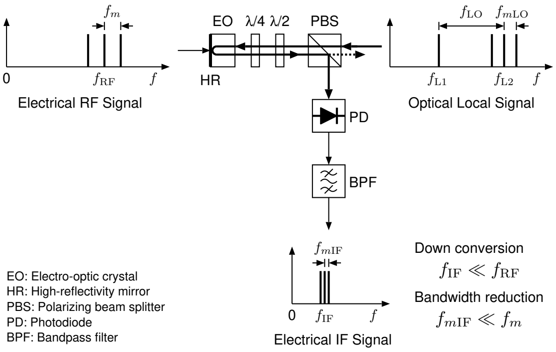

Figure 2. Proposed EO frequency conversion

converted to the IF signal frequency $f_{\mathrm{IF}} = |f_{\mathrm{RF}} - f_{\mathrm{LO}}|$ and the frequency spacing f_m of the IF signal is preserved. An IF signal with wide frequency spacing f_m is affected by the frequency characteristics of electrical circuits downstream from the PD, and a high sampling rate is required to digitize the IF signal.

Figure 2 shows the principle of the proposed EO frequency conversion. One optical CW signal is changed to an optical 3-tone signal with frequency spacing $f_{m\mathrm{LO}}$ set to a slightly different frequency from f_m. The intensity of the optical local signal has three frequency components: f_{LO}, and $f_{\mathrm{LO}} \pm f_{m\mathrm{LO}}$. The RF signal frequencies f_{RF} and $f_{\mathrm{RF}} \pm f_m$ are converted to IF signal frequencies f_{IF} and $f_{\mathrm{IF}} \pm f_{m\mathrm{IF}}$ with a frequency spacing shortened to $f_{m\mathrm{IF}} = |f_m - f_{m\mathrm{LO}}|$. Other frequency components generated by frequency conversion are removed by a bandpass filter (BPF). The IF signal with narrow frequency spacing $f_{m\mathrm{IF}}$ is less susceptible to the frequency characteristics of downstream electrical circuits.

3. Experiment

Figure 3 shows the experimental setup for phase measurement of a mmWave 3-tone signal. In part (a) generating the mmWave 3-tone signal, a 3-tone IF signal generated by an arbitrary waveform generator (AWG) is up-converted using a local frequency of 15.9 GHz × 18, and the upper sideband is extracted by a BPF. A 3-tone RF signal with frequencies of 307.1, 307.2, and 307.3 GHz is input to the EO probe.

In part (b) generating the optical local signal, an optical frequency comb with a spacing of 19.199937375 GHz is generated by a mode-locked fiber laser. The two optical CW signals with a spacing of 307.198998 GHz are extracted by the optical BPFs; one of the two signals is modulated by a $\mathrm{LiNbO_3}$ phase modulator to generate an optical 3-tone signal with a spacing of 99.999996 MHz, and the optical local signal is amplified by an erbium-doped fiber amplifier (EDFA).

The EO probe has a 0.6-mm thick GaAs EO crystal. The 307.2-GHz RF signal f_{RF} with f_m of 100 MHz is converted to a 1.002-MHz 1st IF signal f_{IF} with $f_{m\mathrm{IF}}$ of 4 Hz. Since the signal-to-noise ratio at a frequency range of less than 100 kHz is severely deteriorated by $1/f$ noise at the EO probe outputs, the frequency of the 1st IF signal f_{IF} is set to 1 MHz to avoid $1/f$ noise.

In part (c) performing 2nd frequency conversion and phase detection, the 1st IF signal is converted to an in-phase (I) signal and a quadrature-phase (Q) signal, and the frequencies of the I/Q signals are -2.5, 1.5, and 5.5 Hz. To avoid any impact of DC offset and I/Q imbalance, the frequencies of the I/Q signals are designed to be asymmetric about the zero frequency. The I/Q signals are digitized by A/D converters at 50 sample/s. The phase of the 3-tone I/Q signal is measured by subsequent offline digital signal processing (DSP). First, resampling compensates for sampling timing difference between the I and Q signals.

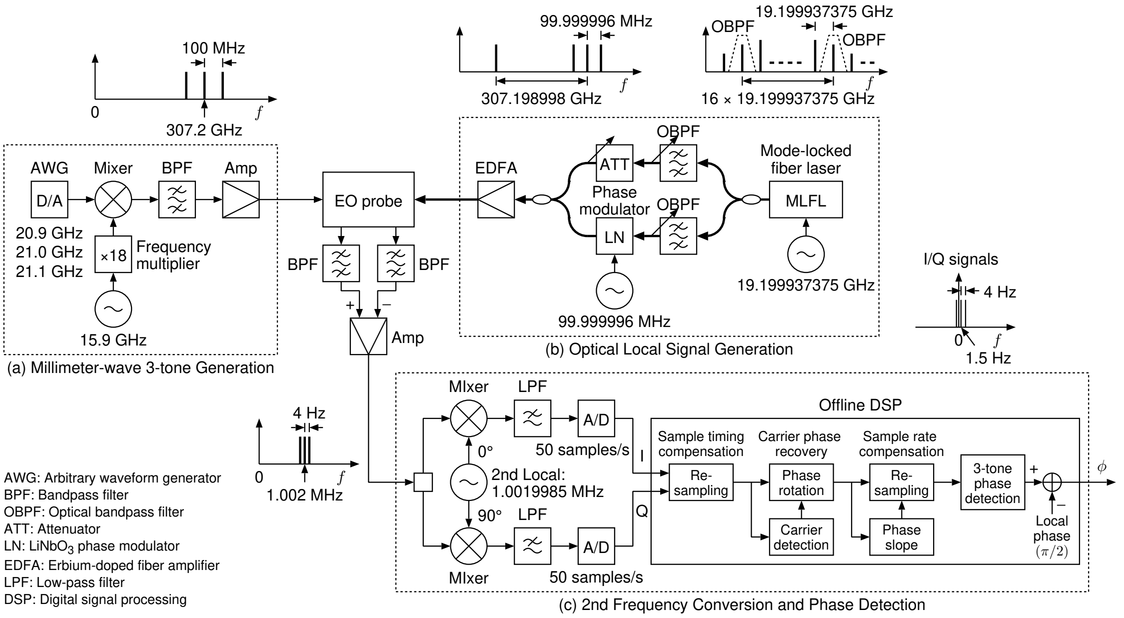

Figure 3. Experimental setup for phase measurement of mmWave 3-tone signal

Since the carrier phase fluctuation is not negligible for mmWave signals, the carrier phase is detected from the 3-tone signal and the carrier phase fluctuation is corrected by phase rotation. The sampling rate error due to the asynchronous A/D conversion clock is compensated for by calculating the phase slope relative to the time and resampling I/Q signals. Finally, the phase of the 3-tone signal is detected and the phase between the three frequencies of the optical local signal is subtracted from the measured phase. The absolute phase and phase tilt in the frequency domain are not obtained by these experiments because the origin of the time axis is indefinite for high-frequency signal measurements. Consequently, at least 3 tones are required for phase measurement. In our experiments, phase ϕ in Eq. (1) was used as the phase measurement result.

$$\phi = \frac{\phi(f_1) - 2\phi(f_2) + \phi(f_3)}{2} \tag{1}$$

where, $\phi(f_1)$, $\phi(f_2)$, and $\phi(f_3)$ are the phases of the 3 tones with frequencies f_1, f_2, and f_3, respectively.

4. Experimental results

The circles in Fig. 4 show the measured phases of the 3-tone RF signals while changing the phase of the 3-tone IF signal. The measurement time span was 512 s. The circles indicating measured phase are different from the dashed line, showing the RF signal phase equals the IF signal phase, and the difference depends on the IF signal phase. This cannot be explained by linear frequency characteristics. Therefore the 3rd-order nonlinear coefficient was estimated by the method shown in Fig. 5. A 3-tone signal with frequencies of 307.15, 307.2, and 307.25 GHz and a phase ϕ of 45° was generated, and the amplitudes at frequencies of 307.1, 307.2, and 307.3 GHz were measured using the experimental setup. The measured 3rd-order intermodulation distortion (IMD) level was -22.9 dB. The 3rd-order nonlinear coefficient was obtained by numerical simulation for 3rd-order nonlinearity showing an IMD level of -22.9 dB. The phase characteristics of the 3-tone RF signal were calculated using the estimated nonlinear coefficient and were plotted as the solid line in Fig. 4. The circles indicating the measured phase agree with the solid line for theoretical phase taking account of 3rd-order nonlinearity.

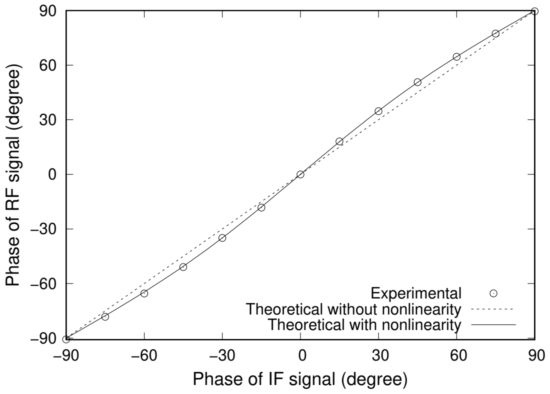

Figure 4. Experimental results of phase measurement

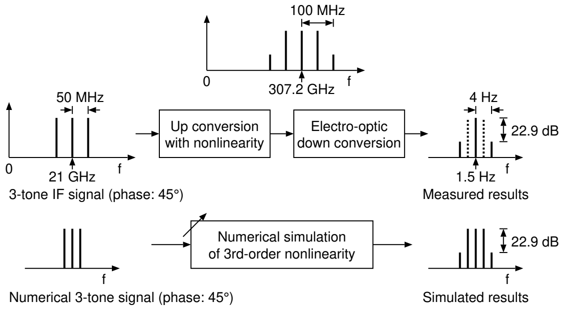

Figure 5. Estimation of 3rd-order nonlinear coefficient

The 512-s phase measurement time span was repeated 12 times to evaluate the precision of the measured phase. The circles in Fig. 6 show the standard deviations for the measured phases using various time spans on acquired data, and the error bars show 95% confidence intervals for the standard deviations. The standard deviation was less than 1 degree for measurement times longer than 8 s.

5. Conclusion

A 300-GHz band 3-tone RF signal was measured by EO frequency conversion using a three-frequency optical local signal. The 3-tone RF signal with 100-MHz spacing was converted to 3-tone I/Q signals with a frequency spacing of just 4 Hz; the I/Q signals were digitized by low-speed A/D converters of 50 sample/s. The phase results measured by varying the phase of the 3-tone signal matched the theoretical phase, taking account of 3rd-order nonlinearity.

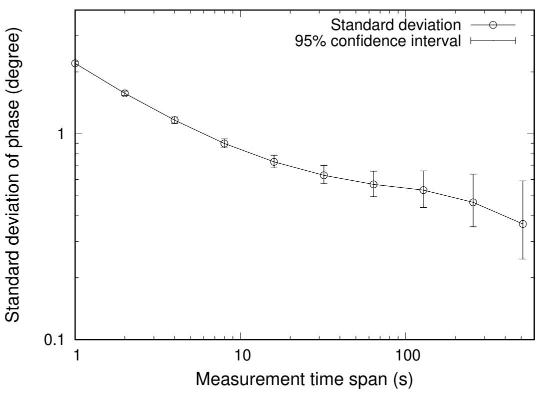

Figure 6. Standard deviation of measured phase

Acknowledgments

This research was supported partly by the Ministry of Internal Affairs and Communications program for expansion of radio-wave resources. We thank the members of the research working group for their valuable advice and opinions.

References

[1] Nagatsuma T. THz communication systems. 2017 Optical Fiber Communications Conference and Exhibition (OFC). Mar. 19–23, 2017. Los Angeles, CA. paper Tu3B.1. pp. 1–90.

[2] Valdmanis JA, Mourou G. Subpicosecond electrooptic sampling: principles and applications. IEEE J Quantum Electron. 1986 Jan;22(1):69–78.

[3] Kolner BH, Bloom DM. Electrooptic sampling in GaAs integrated circuits. IEEE J Quantum Electron. 1986 Jan;22(1):79–93.

[4] Kimura Y, Fuse M, Mattori S, Mori T. Study of Phase Calibration Method of Terahertz-wave Down-converter by Electro-optic Sampling. 2018 IEICE General Conference. Mar. 20–23, 2018. Tokyo, Japan. paper BCI-1-7. pp. SS-87–88.

[5] Sasaki A, Nagatsuma T. Millimeter-wave imaging using an electrooptic detector as a harmonic mixer. IEEE J Sel Topics Quantum Electron. 2000 Sept/Oct;6(5):735–740.

[6] Hisatake S. Visualization of millimeter and terahertz waves based on photonics. 2016 IEEE International Topical Meeting on Microwave Photonics (MWP). Oct. 31–Nov. 3, 2016. Long Beach, CA. paper TuM2.5. pp. 73–74.

[7] Yokoyama S, Nakamura R, Nose M, Araki T, Yasui T. Terahertz spectrum analyzer based on a terahertz frequency comb. Optics Express. 2008 Aug;16(17):13052–13061.

[8] Mori T, Mattori S. Phase Measurement Method for Millimeter-wave 3-tone Signal using Electro-optic Frequency Conversion. IEICE Technical Report. vol. 118. no. 251. Oct. 18–19, 2018. Saga, Japan. paper OCS2018-38. pp. 55–59.